

Hydrodynamic stability and turbulence in fibre suspension flows

by

Mathias Kvik

May 2012
Technical Reports from
Royal Institute of Technology
KTH Mechanics
SE-100 44 Stockholm, Sweden

Akademisk avhandling som med tillstånd av Kungliga Tekniska Högskolan i Stockholm framlägges till offentlig granskning för avläggande av teknologie licentiatexamen den 12 juni 2012 kl 14.00 i Seminarierrummet, Brinellvägen 32, Kungliga Tekniska Högskolan, Stockholm.

©Mathias Kvik 2012

Universitetsservice US-AB, Stockholm 2012

Mathias Kvick 2012, **Hydrodynamic stability and turbulence in fibre suspension flows**

Wallenberg Wood Science Center & Linné Flow Centre
KTH Mechanics
SE-100 44 Stockholm, Sweden

Abstract

In this thesis fibres in turbulent flows are studied as well as the effect of fibres on hydrodynamic stability.

The first part of this thesis deals with orientation and spatial distribution of fibres in a turbulent open channel flow. Experiments were performed for a wide range of flow conditions using fibres with three aspect ratios, $r_p = 7, 14, 28$. The aspect ratio of the fibres were found to have a large impact on the fibre orientation distribution, where the longer fibres mainly aligned in the streamwise direction and the shorter fibres had an orientation close to the spanwise direction.

When a small amount of polyethyleneoxide (PEO) was added to the flow, the orientation distributions for the medium length fibres were found to approach a more isotropic state, while the shorter fibres were not affected.

In most of the experiments performed, the fibres agglomerated into streamwise streaks. A new method was develop in order to quantify the level of agglomeration and the streak width independent of fibre size, orientation and concentration as well as image size and streak width. The width of the fibre streaks were found to correspond well to the width of the well known low velocity streaks found in turbulent boundary layers. Furthermore, the streakiness, *i.e.* the tendency for fibres to agglomerate into streaks, was shown decrease with Reynolds number.

In order to increase the knowledge on the effects of fibres on hydrodynamic stability, experiments in a curved rotating channel was performed with water and a nano-fibrillated cellulose (NFC) suspension. Flow visualisations were used to obtain a stability map as a function of rotation rate and flow rate. The addition of NFC was found to stabilise the primary instability. The effect on the secondary instability was inconclusive, however, no destabilisation was observed.

In addition to the experiments, a linear stability analysis was performed with different volume fractions of fibres using two different stationary orientation distributions. The linear stability analysis was found to under predict the increase in critical Reynolds number compared to the experiments.

Descriptors: Fluid mechanics, fibre suspension, turbulence, image analysis, hydrodynamic stability, nano-fibrillated cellulose.

Preface

In this thesis, fibres in turbulent flows as well as the effect of fibres on hydrodynamic stability are studied. The thesis is divided into two parts. The first part provides an introduction to fibre suspension flows, gives an overview of the experimental setups and summarises the results. The second part consists of three papers;

Paper 1 Mathias Kvik, Karl Håkansson, Fredrik Lundell, Lisa Prah Wittberg and L. Daniel Söderberg;

Fibre orientation and fibre streaks in turbulent wall bounded flow

Paper 2 Karl Håkansson, Mathias Kvik, Fredrik Lundell, Lisa Prah Wittberg and L. Daniel Söderberg;

Measurement of width and streakiness of particle streaks in turbulent flows

Paper 3 Mathias Kvik, Fredrik Lundell, Lisa Prah Wittberg and L. Daniel Söderberg;

Effects of nano-fibrillated cellulose on curvature- and rotation-induced instabilities in channel flow

May 2012, Stockholm

Mathias Kvik

Parts of this work have been presented by the author at:

7th International Conference of Multiphase Flows ¹,
30 May – 4 June 2010, *Tampa, Florida, USA*

3rd SIG43 workshop on fibre suspension flows,
6 – 8 April 2011, *Udine, Italy*

SPCI event,
17 – 19 May 2011, *Stockholm, Sweden*

Svenska mekanikdagarna,
13 – 15 June 2011, *Gothenburg, Sweden*

SIAMUF seminarium.
20 – 21 October 2011, *Gothenburg, Sweden*

Parts of this work have also been presented at:

2nd SIG43 workshop on fibre suspension flows,
9 – 10 February 2010, *Stockholm, Sweden*

Ekmandagarna,
25 – 26 January 2011, *Stockholm, Sweden*

8th International Conference on Flow Dynamics².
9 – 11 November 2011, *Sendai, Japan*

¹With written contribution to the conference proceedings: M. Kvik, K. Håkansson, F. Lundell, L. Prahl Wittberg and L. D. Söderberg: Fibre Streaks in Wall Bounded Turbulent Flow.

²The presentation received a "Best poster" award

The ability to think differently today from yesterday distinguishes the wise man from the stubborn.

– John Steinbeck

Contents

Abstract	iii
Preface	iv
Part I. Overview & summary	1
Chapter 1. Introduction	3
1.1. Industrial motivation	3
1.1.1. Composites & papermaking	3
1.1.2. Fibre orientation & distribution	4
1.2. Particles in flowing fluids	4
1.3. Present work	7
Chapter 2. Fibres in flowing fluids	9
2.1. The motion of fibres in laminar flows	9
2.2. Fibres in turbulent flow	10
2.3. Hydrodynamic stability of fibre suspension flows	10
Chapter 3. Experimental setups, methods & theory	13
3.1. The water table	13
3.2. Curved rotating channel	15
3.2.1. Experimental setup	15
3.2.2. Theoretical considerations	17
Chapter 4. Results & discussion	19
4.1. Fibre orientation	19
4.1.1. Effect of polymers	19
4.2. Fibre streaks	20
4.3. Effect of nano-fibrillated cellulose on stability	21
Chapter 5. Conclusion & outlook	25

Chapter 6. Papers & author contributions	27
Acknowledgements	29
References	31
Part II. Papers	35
Paper 1. Fibre orientation and fibre streaks in turbulent wall bounded flow	39
Paper 2. Measurement of width and streakiness of particle streaks in turbulent flows	61
Paper 3. Effects of nano-fibrillated cellulose on curvature- and rotation-induced instabilities in channel flow	83

Part I

Overview & summary

CHAPTER 1

Introduction

This thesis investigates the behaviour of fibres in turbulent flow as well as the effect of fibres on hydrodynamic stability. The aim is to increase the understanding of the coupling between fibres and turbulent flow. The work is mainly experimental, though comparisons with theory is performed in the part considering the hydrodynamic stability.

The flow of fibre suspensions are of importance in many manufacturing processes. Thus, the first chapter describes a few important aspects as well as some of the difficulties in understanding these processes.

1.1. Industrial motivation

Turbulent fibre suspension flows have been of general interest for a long time, to a large extent due to their connection with papermaking and the manufacturing of composite materials. However, when Toms (1948), as stated by Virk *et al.* (1967), found that the addition of polymers in a turbulent pipe flow resulted in drag reduction, the topic of elongated particles in turbulent flows gained increased attention. Even though this phenomenon is still not fully understood, it is widely used in industry. The reason for this extended use is that a small amount of polymers or fibres can reduce the energy needed to transport fluids, resulting in economical benefits, Virk (1975) reported as much as 80% drag reduction in an experiments with a solution containing 1000 ppm by weight of polyethyleneoxide.

1.1.1. Composites & papermaking

The use of fibres in different kinds of composites is very old, and can be traced back to the Egyptians¹, where mud was mixed with straw in the 15th century BCE in order to increase the strength of the material. A composite is defined as a product consisting of two materials (fibre and matrix), which, when mixed, provides enhanced properties compared to each material on its own. Since the Egyptians first attempts, the manufacturing of composites has of course advanced, although the principles remain. During the 20th century, through the invention of plastic and glass fibre, many of the composites that

¹<http://composite.about.com/>

were previously produced from biodegradable materials were replaced by oil-based composites. In recent years, when concerns regarding the oil supply as well as global warming has risen, the demand for biodegradable and recyclable composites has increased and wood based products has gained an increased interest once again.

Papermaking and the manufacturing of composites shares several aspects due to the use of fibres in both cases, the main difference between the two being that in papermaking there is no matrix present.

1.1.2. Fibre orientation & distribution

In all composite materials and paper, the overall orientation of the reinforcing part (fibres) plays a crucial role in deciding the mechanical properties of the final product. Cox (1952) showed a strong correlation between the fibre orientation and the bending stiffness of paper. Even though the connection between orientation and strength has been known for a long time, no complete explanation has been given to why the fibres end up with a certain orientation. In many industries, an optimal product has been found by trial and error, resulting in that the optimal product actually is not optimal, but simply the best that could be achieved.

The overall spatial distribution of fibres in a composite or a paper, has of course also an impact on the final material, the material will become weaker where there are less fibres, see *e.g.* Norman (2005). This can partly be avoided by the disruption of fibre flocs, which can be present in the suspension. To a wide extent, turbulence has been the mechanism used to break up these flocs, and there are several different methods on how to implement this.

In a paper machine, large turbulent scales are generated by inserting vanes into the headbox, which together with the accelerated flow are used to break up the fibre flocs. However, it has been suggested, *e.g.* by Karema *et al.* (1999), that even though the turbulence generated by these vanes will break the flocs and enhance the mixing in the headbox, the flocs will thereafter reform due to coherent structures forming in the flow. The overall effect of these vanes has not completely been investigated, and there might be more efficient deflocculation methods.

1.2. Particles in flowing fluids

In order to gain understanding of how the fibre orientation and the distribution of the fibres are affected by the flow, it is important to realise that the fibres themselves also affect the flow. When considering particles in a flow, there are several ways to describe how the flow and particle motions are connected. The simplest approach being the one-way coupling, where the particles follow the flow due to the forces acting on the particles, *i.e.* the particles are light. The second is the two-way coupling, where forces are exerted in both directions, *i.e.*

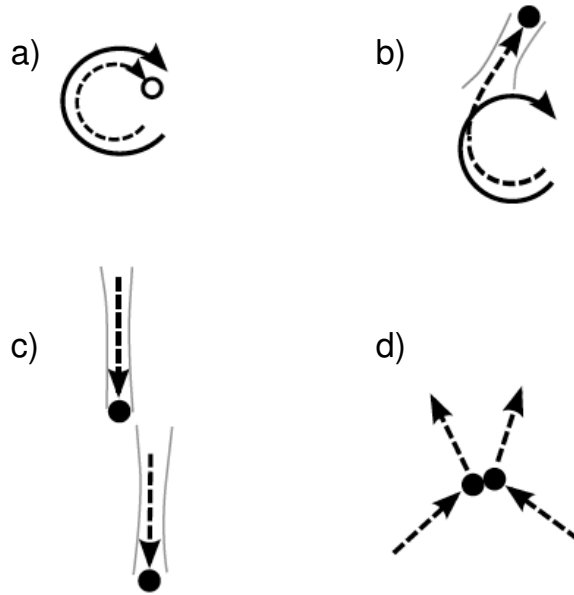


FIGURE 1.1. Interactions between particles and fluid. In a) the particle follows the fluid, in b) the particle has inertia and affects the fluid, in c) additional hydrodynamic interaction between particles are considered, and in d) the particles also collide. In the figure above solid lines are streamlines, dashed lines are particle trajectories, grey lines are wakes behind particles, white dots are light particles and black dots are heavy particles.

the fluid act on the particle and the particle acts back on the fluid, *e.g.* due to wakes behind particles. In a three-way coupling, in addition to what was previously mentioned, the particles interact with each other through hydrodynamic forces, this is of increased importance for larger concentrations. In a four-way coupling, the model is extended to include particle - particle collisions. The four different couplings described here are depicted in figure 1.1, for a more complete description see *e.g.* Crowe *et al.* (1998).

However, when the particles in question are located close to a solid surface, there are more factors that need to be taken into consideration. The mechanical contact between the particle and the wall is of course of importance, but also the hydrodynamic interactions between the particle and the wall needs to be considered.

All of the above mentioned effects, become even more complex when non spherical particles are considered. This is because the rotation of the particle needs to be taken into account since the force transfer for non-spherical particles also will depend on the orientation of the particle.

The non-dimensional numbers describing the flow of a particle suspension are the particle Reynolds number, Re_p , defined as the ratio between the viscous and inertial forces in the near surrounding of the particle and the Stokes number, St , defined by the ratio of the relaxation time of the particle and a relevant timescale of the flow.

It is possible to model the presence of particles in a fluid, spherical or non-spherical, as an effect on rheological the bulk properties instead of accounting for each individual particle. The rheology of a fluid describes how the fluid reacts when a force is applied. For a Newtonian fluid this is described by a single parameter, *i.e* the temperature dependent viscosity. When particles are added to the fluid, more complex relations between the stress and strain rate are obtained. When fibres are considered, this model consists of an additional stress coupled with the orientation tensor, a tensor related to the fibre orientation distribution, see *e.g.* Advani & Tucker III (1987) and Batchelor (1970*b*). The reason for the coupling between the orientation and the stress, is that a fibre suspension will be able to resist different amount of force in different directions depending on the local fibre orientation. This is directly related to what was previously discussed concerning the manufacturing of composites, where the orientation of the fibres in the matrix to a large extent decides the strength of the final composite in different directions.

The above implies that the fibre orientation distribution needs to be known explicitly in order to calculate the stress, which is not possible in many cases when complex flow fields are of interest. The calculation of the orientation distribution is usually avoided by obtaining fourth order orientation tensors which is a function of the flow. However, this fourth order tensor will depend on the sixth order tensor and so on, leading to a closure problem similar to that found for the Reynolds stresses in turbulence. In order to overcome this closure problem, a closure approximation is needed. Petrie (1999) reviewed many of the closure approximations that have been suggested and in detail explains what needs to be considered when constructing a rheological model.

In addition to the modelling of the rheology not being trivial, to measure the viscosity of fibre suspensions is in itself not an easy task and the literature regarding shear viscosity measurements is scarce. For a review of what has been accomplished in this area see *e.g.* Derakhshandeh *et al.* (2011), where a short section handles the shear viscosity of fibres suspensions. Derakhshandeh *et al.* (2011) points out, that even though there is a lack of experiments regarding the shear viscosity of cellulose fibre suspensions, more work has been done using other types of fibres, and there are similarities that can be exploited.

1.3. Present work

The increased accuracy in the modelling of fibre suspensions, by the coupling of DNS and fibre motions, calls for quantitative experimental data to be used in the validation process. In order to provide data regarding fibres in turbulent wall-bounded flow as well as investigating differences from laminar flow, the effects of different flow- and fibre-parameters on orientation distributions and spatial distributions are investigated in this work.

Two experiments have been performed. In the first, fibre orientation and spatial distribution in a turbulent flow are studied. Detailed orientation measurements for a wide parameter space are given. Furthermore, the tendency for fibres to form streaks is carefully quantified.

The second experiment concerns flow instabilities in a curved rotating channel. Nano-fibrillated cellulose (nanometer sized cellulose fibrils derived from pulp) is added to the flow and the effects on the stability is investigated. The experimental observations are compared to linear stability analysis.

CHAPTER 2

Fibres in flowing fluids

In this chapter, a short review is provided regarding the basics of fibres in flowing suspensions.

2.1. The motion of fibres in laminar flows

When Jeffery (1922), derived the equations of motion for an ellipsoidal particle in simple shear, this was a first step toward understanding how fibres behave in different flows. The rotational velocities for an ellipsoidal particle in simple shear are given by:

$$\dot{\phi} = -\frac{\dot{\gamma}}{r_e^2 + 1}(r_e^2 \sin^2 \phi + \cos^2 \phi), \quad (2.1)$$

$$\dot{\theta} = \left(\frac{r_e^2 - 1}{r_e^2 + 1}\right) \frac{\dot{\gamma}}{4} \sin 2\phi \sin 2\theta, \quad (2.2)$$

where $\dot{\gamma}$ is the shear rate, r_e the aspect ratio for the ellipsoidal particle, θ the angle between the vorticity axis and the major axis of the ellipsoid and ϕ is the angle between the flow-vorticity plane and the plane made up by the major axis of the particle and the vorticity axis.

The work by Jeffery (1922) has been verified several times, *e.g.* Trevelyan & Mason (1951), who studied the motion of spherical and cylindrical particles in a Couette flow experimentally. Goldsmith & Mason (1962) expanded the previous mentioned study by investigating the effect of a varying velocity gradient in Poiseuille flow. In these experimental studies, cylindrical rods were used. The results provided an equivalent aspect ratio by assuming a rotation time equal to the analytical solution for an ellipsoidal particle as was reported by Jeffery (1922). Harris & Pittman (1975) presented the following empirical formula:

$$r_e = 1.14r_p^{0.844}, \quad (2.3)$$

to be the best fit to their experimental data for values of r_p between 1 and 120, where r_p is the aspect ratio of the cylindrical particle.

The equations of motion for spheroids have later been derived for any body of revolution by Bretherton (1962), and for bodies with arbitrary cross sections by Batchelor (1970*a*). In recent years, the effects of particle- and fluid-inertia

has become an area of interest. Two recent examples are Subramanian & Koch (2006), who studied the effects of fluid and particle inertia on almost spherical particles and Lundell & Carlsson (2010) where the effect of particle inertia on ellipsoids in Stokes flow were scrutinised.

2.2. Fibres in turbulent flow

Even though the motion of spheroids has been studied for almost a century, it is not until recently, when direct numerical simulations (DNS) of turbulent fibre suspension flows has become feasible to perform, that numerical results are of interest to use in more complex applications with high accuracy. Zhang *et al.* (2001) was first to perform a DNS coupled in one direction with the equations of motion for non-spherical particles in a turbulent channel flow. The equations of motion included hydrodynamic forces, torques, shear induced lift and gravitational forces. The numerical methods since then have been developed to also include inertia by Mortensen *et al.* (2008). Marchioli *et al.* (2010) extended the parameter range in terms of aspect ratios and particle response time. Andersson *et al.* (2012) developed a torque-coupling scheme between Lagrangian point-particles and an Eulerian fluid, and applied the method on a particle laden turbulent channel flow.

As more detailed results from numerical simulations emerges, the demand for detailed experimental results to be used in the validation process has increased. Of interest are orientation of the fibres and their translational- and rotational velocities. This information is necessary to be able to compare statistical data as well as providing possible explanations for the mechanisms responsible for the fibre orientation.

2.3. Hydrodynamic stability of fibre suspension flows

The effects of fibres on the transition from laminar to turbulent flow, is an area that has not received the attention needed. The few experiments that have been performed are not conclusive and indicate that fibres can stabilise certain instabilities while destabilising other.

Vaseleski & Metzner (1974) measured pressure drops in pipes of different diameters in order to investigate drag reduction of suspensions containing various volume fractions and aspect ratios of nylon fibres. They found that the transition to turbulence was delayed, *i.e.* the flow was stabilised due to the presence of fibres. Pilipenko *et al.* (1981) on the other hand, found that the addition of plant fibres in a Taylor apparatus decreased the critical Taylor number and thereby destabilised the flow.

Theoretical results within this area are more coherent and suggests that fibres have a stabilising effect on various flows. Gupta *et al.* (2002) studied the transition in the Taylor-Couette flow of a semi-dilute, non-Brownian, fibre

suspension by means of a linear stability analysis, and came to the conclusion that regardless of closure approximation for the orientation tensor, the critical Reynolds number increased. Moreover, fibre-fibre interactions, modelled by an interaction coefficient, were proposed to be the main reason for this stabilisation. Nsom (1996) investigated the effect of fibres and gap-width on the stability of a Dean flow. The critical wavelength was determined to be unaffected by the presence of fibres, while the transition to turbulence was delayed both in the dilute and semi-dilute regime. Azaiez (2000) performed a linear stability analysis of a mixing layer containing fibres and found that the orientational diffusivity due to hydrodynamic interactions was the main reason for stabilisation. Similar results were reported by Zhenjiang *et al.* (2004) who studied the linear stability of a fibre suspension in two-dimensional channel flow and found that the addition of fibres stabilised the flow but also had an effect on the critical wavenumber, which is contradicting previously mentioned results by Nsom (1996).

Due to the lack of experimental work to validate the simulations, no quantitative results are available. Furthermore, contradictions such as Vaseleski & Metzner (1974) vs Pilipenko *et al.* (1981), where one reports that fibres acts stabilising and the other destabilising, indicate that there is a lack of knowledge regarding the appropriate modelling of the effects of fibres on hydrodynamic stability. The reason for the few experimental studies are possibly due to the difficulty to determine the rheological properties of the suspension for a relevant situation, where for example a measurement of the shear viscosity is not enough to decide the properties of the fluid. Furthermore, there are several parameters that are difficult to control in the experiments, such as distribution (particles tend to form clusters) and orientation of the fibres. In addition, measuring fluid velocity in a dense fibre suspension is difficult due to the lack of optical access.

CHAPTER 3

Experimental setups, methods & theory

In this chapter, two experimental setups and the techniques used in acquisition and analysis of data are described, as well as the theory used to model the effect of fibres the hydrodynamic stability in a curved rotating channel. For a more detailed description the reader is referred to the papers in Part II.

3.1. The water table

In order to increase the understanding of the behaviour of fibres in turbulent boundary layers and obtain data that can be used as validation for numerical simulations, cellulose acetate fibres are introduced into a half channel flow, Kvick *et al.* (2012a). The experimental setup consists of a water table and a camera, displayed in figure 3.1. The water is pumped from a downstream reservoir to an upstream reservoir, allowing the suspension to flow down the inclined glass plate. The camera is placed at a position more than 100 heights of the water layer downstream of the inlet, where images of all the fibres in the region of interest in the flowing suspension are acquired through the glass plate.

The fibres in the images are identified using a second order ridge detector within the class of steerable filters, Carlsson *et al.* (2011), providing the position and orientation for each individual fibre in the flow-vorticity plane.

Since the flow down the inclined glass plate is driven by gravity alone, it is possible to calculate the wall shear stress, τ_w , through the force balance between the water and the plate;

$$\tau_w = \rho g h \sin \alpha, \quad (3.4)$$

where ρ is the density of water, g is the gravitational acceleration, h is the height of the water layer and α is the inclination angle of the glass plate defined positive in the clockwise direction with $\alpha = 0$ in the direction of the x-axis. This is a half channel flow, and the friction Reynolds number, Re_τ , is typically defined as;

$$\text{Re}_\tau = \frac{h}{\nu} u_\tau = \frac{h}{\nu} \sqrt{\frac{\tau_w}{\rho}} = \frac{h \sqrt{g h \sin \alpha}}{\nu}, \quad (3.5)$$

where u_τ is the friction velocity and ν is the kinematic viscosity. The non-dimensional numbers describing particles in the flow are the particle Reynolds

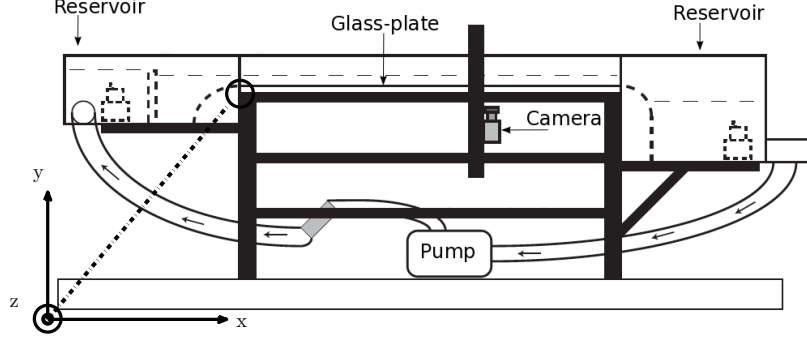


FIGURE 3.1. Schematic of the water table.

number, Re_p , defined as the ratio between the viscous and inertial forces in the near surrounding of the particle and the Stokes number, St , defined by the ratio of the relaxation time of the particle and a relevant timescale of the flow or equally by the density ratio times Re_p . Re_p is defined as, Aidun *et al.* (1998);

$$Re_p = \dot{\gamma} \frac{l_f^2}{\nu} = \frac{\tau_w l_f^2}{\rho \nu} = \frac{l_f^2 g h \sin \alpha}{\nu^2}, \quad (3.6)$$

where $\dot{\gamma}$ represents the shear rate at the glass plate and l_f is the fibre length. An equivalent Stokes number, St , can be calculated by multiplying Re_p with the density ratio of the particles and the fluid, Lundell & Carlsson (2010). The physical water layer thickness, h , is 8–12 mm depending on parameter combination. In the experiments, Re_τ is varied between 50 and 210, which corresponds well with the low Reynolds number turbulence in which DNS are performed, and Re_p is varied between 10 and 10^3 .

The fibres used in the experiments are cellulose acetate fibres with a density of $\rho_f = 1300 \text{ kg/m}^3$, with lengths of $l_f = 0.5, 1, \text{ and } 2 \text{ mm}$. The concentrations of fibres used in the experiment is relatively low, 0.00042 – 0.0033% by weight (corresponding to a number density of $nl^3 = 0.0008 - 0.0066$), where n is the number of fibres per unit volume. Since the fibres are sedimenting in the flow, most of the fibres will be located close to the plate when reaching the position where the images are acquired.

A typical image acquired during one of the experiments is displayed in figure 3.2. It shows an instantaneous image of the black fibres in the flow at the acquisition point, located 1100 mm downstream of the inlet of the glass plate. The orientation of the fibres as well as their non-uniform distribution will be discussed later.

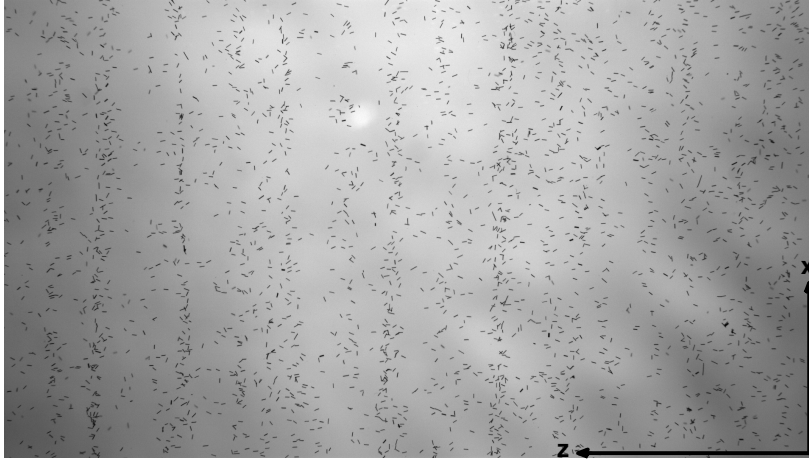


FIGURE 3.2. Typical image of the fibre suspension acquired during experiment. The flow is in the positive x -direction. The black dyed fibres can clearly be seen in the flow.

3.2. Curved rotating channel

3.2.1. Experimental setup

The experimental setup, sketched in figure 3.3, was previously used by Matsson & Alfredsson (1990). The setup consists of a rectangular curved channel that covers 180° and has a radius of curvature $Ra = 400$ mm. Before the contraction at the inlet, packed spheres are placed in order to increase the pressure drop and break up large turbulent scales.

The flowing fluid in the setup is, apart from the driving pressure force, under the influence of two different forces; (i) a centrifugal force due to curvature and (ii) a Coriolis force due to rotation. These two forces are both destabilising by themselves. However, depending on fluid velocity, U_b , angular velocity, Ω , kinematic viscosity ν and channel width, d , the forces can either enhance the destabilisation or counteract each other. The two governing non-dimensional parameters this are the Reynolds number, Re , and the rotational number, Ro , defined as;

$$Re = \frac{U_b d}{\nu}, \quad (3.7)$$

$$Ro = \frac{\Omega d}{U_b}. \quad (3.8)$$

Re is varied between 300 and 800 based on the viscosity of water, and Ro is in the interval $[-0.2, 0.2]$, where positive values of Ro indicate that the channel is rotating in the direction of the flow.

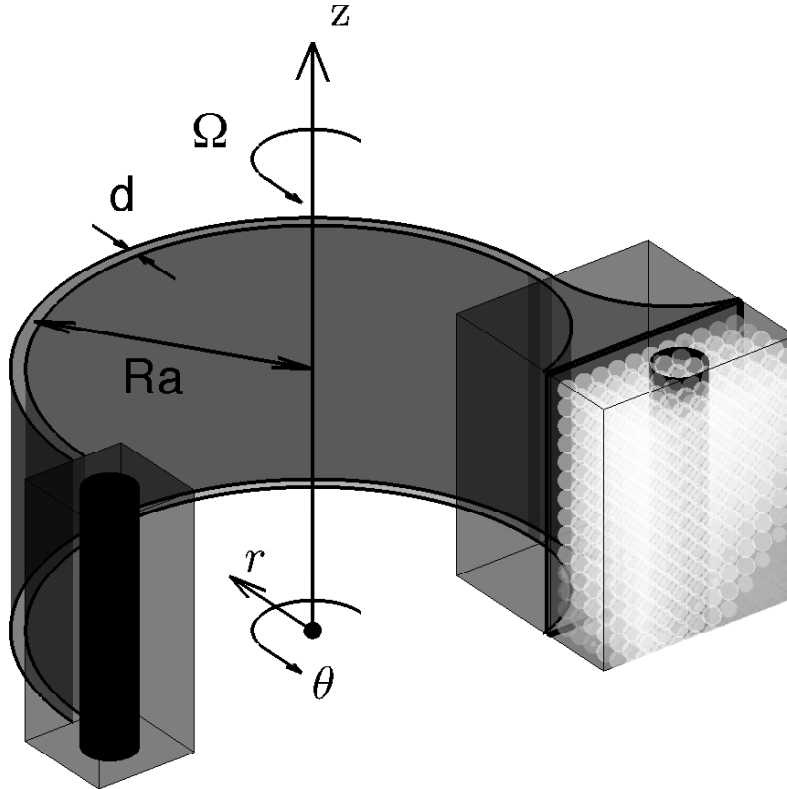


FIGURE 3.3. Sketch of the curved channel. The inlet is to the right in the image, packed spheres, a screen and a contraction are used to reduce the turbulence in the beginning of the channel.

In order to visualise the flow, a small amount of Iridin (plate like particles that visualise flow structures) is added to the fluid. A CCD camera placed at a position of 65 channel widths downstream of the inlet captures images of the flow structures. The images are analysed by visual examination and assigning the set of images to one of six flow regimes: *laminar*, *weak primary instability*, *strong primary instability*, *weak secondary instability*, *strong secondary instability* and *turbulent*.

3.2.2. Theoretical considerations

The flow in the curved rotating channel is governed by the Navier-Stokes equations together with the continuity equation in cylindrical coordinates;

$$\frac{Du_r}{Dt} - \frac{u_\theta^2}{r} = -\frac{1}{\rho} \frac{\partial p}{\partial r} + \nu \left[\nabla^2 u_r - \frac{u_r}{r^2} - \frac{2}{r^2} \frac{\partial u_\theta}{\partial \theta} \right] + 2u_\theta \Omega, \quad (3.9)$$

$$\frac{Du_\theta}{Dt} + \frac{u_r u_\theta}{r} = -\frac{1}{\rho r} \frac{\partial p}{\partial \theta} + \nu \left[\nabla^2 u_\theta - \frac{u_\theta}{r^2} + \frac{2}{r^2} \frac{\partial u_r}{\partial \theta} \right] - 2u_r \Omega, \quad (3.10)$$

$$\frac{Du_z}{Dt} = -\frac{1}{\rho} \frac{\partial p}{\partial z} + \nu \nabla^2 u_z, \quad (3.11)$$

$$\frac{\partial u_r}{\partial r} + \frac{u_r}{r} + \frac{1}{r} \frac{\partial u_\theta}{\partial \theta} + \frac{\partial u_z}{\partial z} = 0, \quad (3.12)$$

where;

$$\frac{D}{Dt} = \frac{\partial}{\partial t} + u_r \frac{\partial}{\partial r} + \frac{u_\theta}{r} \frac{\partial}{\partial \theta} + u_z \frac{\partial}{\partial z}, \quad (3.13)$$

$$\nabla^2 = \frac{\partial^2}{\partial r^2} + \frac{1}{r} \frac{\partial}{\partial r} + \frac{1}{r^2} \frac{\partial^2}{\partial \theta^2} + \frac{\partial^2}{\partial z^2}, \quad (3.14)$$

and the velocity vector is given by;

$$\mathbf{u} = u_r \mathbf{e}_r + u_\theta \mathbf{e}_\theta + u_z \mathbf{e}_z. \quad (3.15)$$

When fibres are added to the flow, an additional term appears in the stress tensor of the form;

$$\boldsymbol{\sigma} = -p\delta_{ij} + 2\mu\boldsymbol{\varepsilon} + \mu_{fibre}\boldsymbol{\varepsilon} \langle \mathbf{p}\mathbf{p}\mathbf{p}\mathbf{p} \rangle, \quad (3.16)$$

where μ is the viscosity of the suspending fluid, μ_{fibre} is a rheological parameter dependent on concentration and aspect ratio of the fibres, $\boldsymbol{\varepsilon}$, is the strain rate tensor and \mathbf{p} is the orientation vector for the fibre.

The fourth order orientation tensor, $\mathbf{a}_4 = \langle \mathbf{p}\mathbf{p}\mathbf{p}\mathbf{p} \rangle$, in equation 3.16, is dependent on the sixth order orientation tensor, and so on, where $\langle \rangle$ denotes the ensemble average. This closure problem is analogue to the closure problem for the Reynolds stresses in turbulence. It is necessary to make an approximation in order to close these equations, this closure can be performed in many different ways, see *e.g.* Petrie (1999). In the present study this approximation is avoided by assuming that all fibres are performing Jeffery orbits in the $r\theta$ -plane, providing the possibility to calculate the fibre orientation distribution and thereby obtaining the necessary terms in the orientation tensor.

Assuming perturbations of the form;

$$u'_r = R(r)e^{i\beta z + st} \quad (3.17)$$

$$u'_\theta = \Theta(r)e^{i\beta z + st}, \quad (3.18)$$

$$u'_z = Z(r)e^{i\beta z + st} \quad (3.19)$$

$$\frac{p'}{\rho} = P(r)e^{i\beta z + st}, \quad (3.20)$$

where β is the spanwise wavenumber and s the temporal growth rate, it is possible to obtain the linear stability equations for the fibre suspension flow. Using the narrow gap approximation, $\gamma = \frac{d}{Ra} \ll 1$ and thus neglecting terms of order γ^2 and higher, this results in the following system of equations;

$$\begin{aligned} & 4(D^2 - \beta^2)^2(1 + \gamma\eta)R + 4\gamma D(D^2 - \beta^2)R - 2\beta^2 \text{Re}(\gamma\mathcal{V} + \text{Ro}(1 + \frac{\gamma}{2}\eta))\Theta + \\ & + A\Phi \left[4a_{rrrr}\beta^2 D^2(1 + \gamma\eta)R + 2\gamma a_{rrrr}\beta^2 DR + \right. \\ & \left. + 4a_{rrr\theta}\beta^2 D^2(1 + \gamma\eta)\Theta - 2\gamma a_{r\theta\theta\theta}\beta^2 D\Theta \right] = \\ & = 2s\text{Re}(D^2 - \beta^2)(1 + \gamma\eta)R + \gamma s\text{Re}DR + \mathcal{O}(\gamma^2), \end{aligned} \quad (3.21)$$

$$\begin{aligned} & 4(D^2 - \beta^2)(1 + \gamma\eta)\Theta + 2\gamma D\Theta - \text{Re}(2\mathcal{V}' + 4\text{Ro})(1 + \gamma\eta)R - \gamma\text{Re}\mathcal{V}R + \\ & + A\Phi \left[4a_{rrr\theta}D^2(1 + \gamma\eta)R + 4\gamma a_{rrr\theta}DR + 2\gamma a_{r\theta\theta\theta}DR + \right. \\ & \left. + 4a_{rr\theta\theta}D^2(1 + \gamma\eta)\Theta \right] = \\ & = 2s\text{Re}(1 + \gamma\eta)\Theta + \mathcal{O}(\gamma^2), \end{aligned} \quad (3.22)$$

where $D = \partial/\partial\eta$, $\mathcal{V} = V/U_b$ is the non-dimensional mean streamwise velocity, $\eta = \frac{z}{\gamma}(\frac{r}{Ra} - 1)$ is the non-dimensional spanwise coordinate, A is a rheological parameter, see *e.g.* Batchelor (1971), Φ is the volume fraction of fibres and a_{ijkl} are elements in the fourth order orientation tensor where only non-zero elements remains in the equation assuming all fibres are located in the $r\theta$ -plane. Solving this eigenvalue problem for s , where real positive values of s indicates a growth of the disturbances, results in critical wavenumbers, β_{cr} , Reynolds numbers, Re_{cr} and rotational numbers Ro_{cr} .

CHAPTER 4

Results & discussion

In this chapter, the author's contribution regarding fibre orientation and formation of fibre streaks in turbulent channel flow as well as the effect of fibres on curvature- and rotation-induced stability are summarised.

4.1. Fibre orientation

In the experiments on the water table it is found that the most important parameter controlling the fibre orientation close to a wall is the fibre length. In figures 4.1a - 4.1c, fibre orientation distributions for three different fibre lengths and different friction Reynolds numbers are displayed. The fibre orientation angle β is defined with $\beta = 0$ in the streamwise direction. For all fibre orientation distributions, orientations for fibres in 150 images with 150 - 1500 fibres in each image is used. This is found to be sufficient to achieve convergence for all cases.

As it is evident from figures 4.1a - 4.1c, the longer fibres with aspect ratio $r_p = 28$ are mostly aligned in the flow direction while the shorter fibres with aspect ratio $r_p = 7$ have an orientation close to the spanwise direction. The medium sized fibres, with aspect ratio $r_p = 14$, assumes a more isotropic distribution. Carlsson *et al.* (2007) and Carlsson (2009) reported similar experimental results for a laminar flow. The reason of the difference in orientational behaviour was suggested to be a competition between effects of sedimentation towards the wall, direct wall interaction and fluid inertia. Moreover, this theory was strengthened by a numerical investigation.

4.1.1. Effect of polymers

A small amount of polyethyleneoxide (PEO) is added to the flow, viscosity measurements of the fluid phase shows that the small amount had no effect on the bulk shear viscosity. The anisotropy, defined as $A = a_{11}/a_{22}$, where a_{ii} are the diagonal components in the second order orientational tensor, Advani & Tucker III (1987), is used to quantify differences in orientation. In figure 4.1d, the suspensions containing PEO, (\square , ∇), are compared to the corresponding reference case, (\blacksquare , \blacktriangledown), where water is the carrying fluid phase. The addition of PEO does not notably effect the anisotropy for the shorter fibres with $r_p = 7$ (\square). However for the fibres of medium length with $r_p = 14$ (∇), the anisotropy

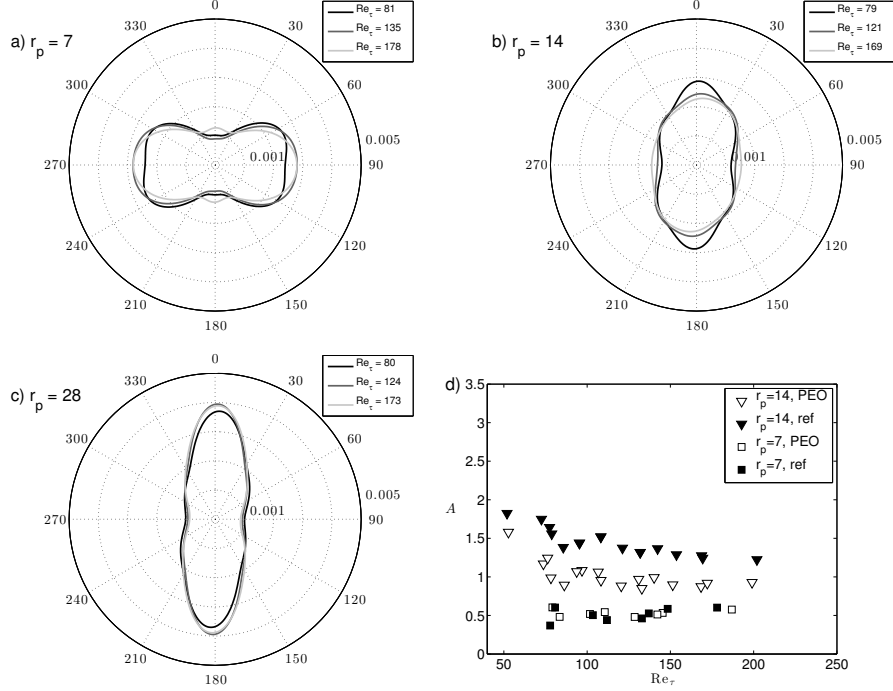


FIGURE 4.1. Fibre orientation distributions for (a) $r_p = 7$, (b) $r_p = 14$ and (c) $r_p = 28$ at different friction Reynolds numbers. d) Anisotropy for suspension containing PEO (∇ and \square) compared to the reference (\blacktriangledown and \blacksquare) where the fluid phase is tap water.

is lower in all cases. The reason for the difference in the result for different fibre aspect ratio is believed to be related to the location of the polymers in the flow. White *et al.* (2004) found that the addition of polymers in a turbulent boundary layer had an effect in the buffer layer, at heights between $5l^+ - 30l^+$, where $l^+ = \nu/u_\tau$ is the viscous length scale, see *e.g.* Pope (2000). Since the length of the fibres with aspect ratio $r_p = 14$ ($l_f = 6l^+ - 18l^+$) corresponds to the location of the buffer layer, while the shorter fibres with aspect ratio $r_p = 7$ have a length ($l_f = 3l^+ - 9l^+$) which is close to the height of the viscous sublayer, the addition of polymers are believed to only affect the fibres located in the buffer layer.

4.2. Fibre streaks

In most of the experiments the fibres agglomerated into streamwise streaks, as observed in the image in figure 3.2. In order to quantify the fibre streaks, a

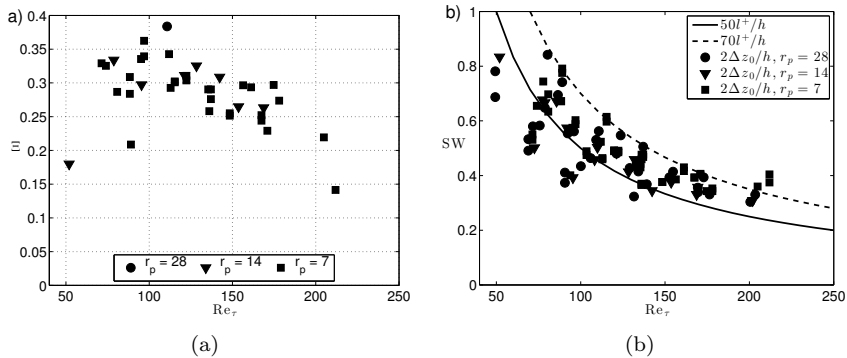


FIGURE 4.2. (a) Relative streakiness, Ξ , as function of Re_τ for different fibre aspect ratios. (b) Normalised streak widths for $r_p = 28$ (\bullet), $r_p = 14$ (\blacktriangledown) and $r_p = 7$ (\blacksquare) where $50 l^+/h$ (full line) and $70 l^+/h$ (dashed line) are shown for comparison.

correlation based method using the positions of the fibres is used, described in Håkansson *et al.* (2012). The lack of data for the longer fibres with $r_p = 28$ in figure 4.2a are due to the results not converging due to lack of images. In figure 4.2a, the relative streakiness, Ξ , a measure of how strong the tendency for the fibres to agglomerate into streaks are, is shown versus the friction Reynolds number for different fibre aspect ratios. As can be observed, there is a maximum of the streakiness at $Re_\tau \approx 110$. The width of the fibre streaks is in figure 4.2b compared to the empirical value of $50l^+$ of low velocity streaks in turbulent boundary layers, Zacksenhouse *et al.* (2001). The streaks are seen to scale in the same manner, although most fibre streaks are wider than the low velocity streaks. Similar results has been reported earlier, Zhao *et al.* (2010) found that the addition of spherical particles caused the velocity streaks to widen.

4.3. Effect of nano-fibrillated cellulose on stability

Example images from four of the six different regimes (laminar, weak primary instability, strong primary instability, weak secondary instability, strong secondary instability and turbulent), used in the analysis of the images acquired of the flow structures in the curved rotating channel, are shown in figure 4.3 for the Newtonian case. In figure 4.3a an example of the laminar case, for $Re = 595$ and $Ro = -0.024$, can be seen, with almost no change in image intensity. Indicating that there are no flow structures present. Increasing the rotational number to $Ro = 0.006$, the primary instability is reached in figure 4.3b with its well defined streamwise vortices. In figure 4.3c and 4.3d, as the rotational number is increased further to $Ro = 0.039$ and $Ro = 0.076$, the vortices break down. This is considered to be a sign of the secondary instability. A further

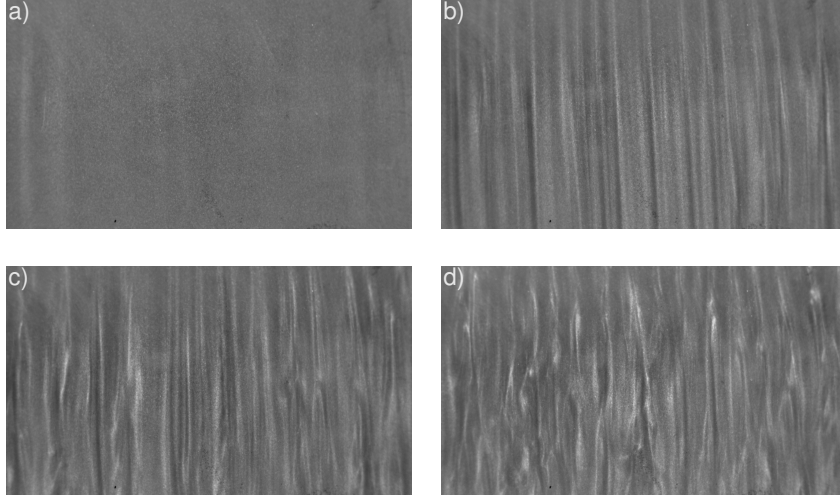


FIGURE 4.3. Example images for a) laminar, b) strong primary instability, c) weak secondary instability and d) strong secondary instability regimes, with $Re = 595$ and $Ro = -0.024, 0.006, 0.039$ and 0.076 respectively.

increase in Ro leads to turbulence. Evidently, the primary instability is quite easy to distinguish whereas the second transition point is more difficult to pinpoint. In the images in figure 4.3, the background for a laminar case with the same flow conditions have been subtracted in order to increase the visibility of the structures in the flow.

In figure 4.4, the results from the visual inspection has been summarised in two plots showing the regime each case belongs to for the Newtonian fluid and the nano-fibrillated cellulose (NFC) suspension in the Re - Ro -plane. In the figure the following notation is used; laminar (\circ), weak primary instability (\times), strong primary ($*$), weak secondary instability (\square), strong secondary instability (∇) and turbulent (\diamond). The Reynolds number in the two figures is based on the viscosity of the suspending fluid. The most obvious difference between figures 4.4a and 4.4b is that in the case of NFC suspension, the secondary instability is never reached.

Figure 4.5a depicts the contours of the first and second transition for the case of the Newtonian fluid as well as the first transition for the NFC suspension. The results presented here are not trivial to analyse. The viscosity of the NFC suspension is in reality greater than that of the the suspending fluid, in addition it is also shear thinning. The shear viscosity versus the shear rate can be found in Kvik *et al.* (2012b), where $\mu_s = 1.8\mu_l$ can be taken as an approximate value, where μ_s and μ_l are the viscosities of the suspension and

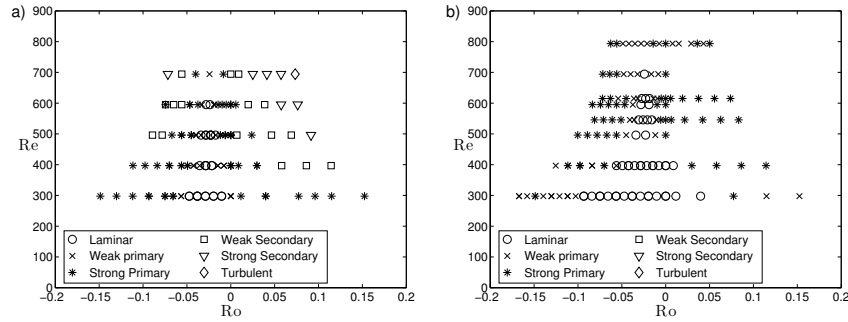


FIGURE 4.4. State diagrams for a) Newtonian fluid and b) NFC suspension. The Reynolds number is in both figures based on the viscosity of water.

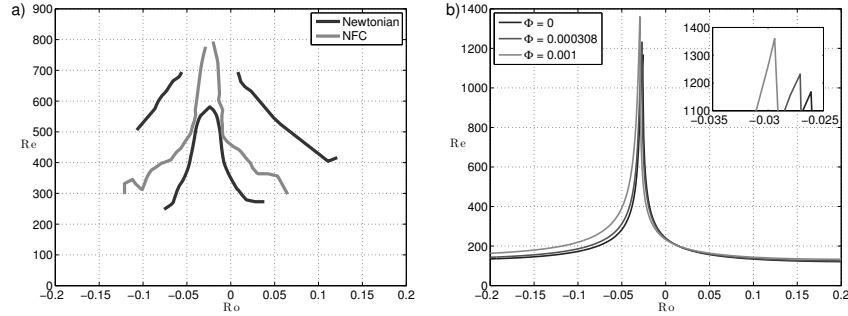


FIGURE 4.5. a) Contours showing the onset of the primary and secondary instability for the Newtonian and NFC-suspension. The Reynolds number is based on the viscosity of water. b) Neutral stability curve obtained by linear stability analysis for different volume fraction of fibres, Φ .

the suspending liquid, respectively. If this viscosity were to be applied on the curve in figure 4.5a, this implies that the fibres are acting as a destabiliser. However, since the orientation of the fibres are unknown in the channel as well as in the rotational viscometer, this conclusion lacks support. Instead, using an effective viscosity of $\mu_s = 1.4\mu_l$ would collapse these two curves onto each other.

Considering that the orientation in the viscometer is random (mixing took place between each measurement) and using the fact that fibres aligned parallel to the vorticity axis would have no effect on the shear viscosity, it is possible to state that the effective viscosity will have a value in the interval $1\mu_l < \mu_s <$

$1.8\mu_l$. The correct value of this viscosity can not be found until the orientation of the fibres in the flow and the velocity in the channel are known.

Figure 4.5b shows the neutral stability curve in the Re-Ro-plane for different volume fractions, Φ , of fibres obtained by a linear stability analysis. It is in this case assumed that the fibres are performing Jeffery orbits in the $r\theta$ -plane given an aspect ratio $r_p = 340$ and an interaction coefficient $C_l = 0.05$, resulting in a effective viscosity of $\mu_s = 1.4\mu_l$. As evident, an increased concentration of fibres causes an increase in the critical Reynolds number. Furthermore, the fibres also seem to affect critical rotational number, where a suspension containing high concentration of fibres demands a larger Coriolis force in order to be stabilised.

Although there are several simplifications in the modelling of the effect of fibres in the linear stability analysis, the curves in figure 4.5a and 4.5b show some interesting similarities. The location of the peak are for both cases located close to $Ro = -0.03$, although the value at the peak are much greater in the case of linear stability. This difference is most likely due to the fact that the inlet conditions in the experiment may not be completely laminar.

CHAPTER 5

Conclusion & outlook

In this thesis the orientation and distribution of fibres in a turbulent channel flow are studied as well as the effect of nano-fibrillated cellulose on curvature- and rotation-induced stabilities.

Regarding the behaviour of fibres in a turbulent wall bounded flow, it is found that, independent of flow conditions, the fibre orientation distribution was to a large extent decided by the aspect ratio of the fibres. Fibres with a large aspect ratio tended to align in the flow direction, while the fibres with a smaller aspect ratio ended up with an orientation close to the spanwise direction. The reason for this was suggested to be a competition between effects of sedimentation towards the wall, direct wall interaction and fluid inertia.

When a small amount of PEO (polyethyleneoxide) was added to the flow, this had a consistent impact of the fibre orientation, driving the distribution toward a more isotropic state. The effect was found to depend on the aspect ratio of the fibres and is believed to occur when the length of the fibres and the position of the buffer layer coincide, since polymers are known to have an effect on the flow in the buffer layer.

The fibre streaks that were seen in the experiments were found to have a width which scaled similarly to the low velocity streaks that can be found in turbulent boundary layers. The width of the fibre streaks were slightly wider than the low velocity streaks. Furthermore, the tendency for the fibres to agglomerate into streaks (*i.e.* the streakiness) was found to decrease with increased Reynolds number.

When NFC (nano-fibrillar cellulose) fibres were added to the flow in a curved rotating channel this was found to have a large stabilising effect on the flow. The magnitude of the stabilisation could neither be predicted by viscosity measurements nor from results obtained by a linear stability analysis. Furthermore, the results from the viscosity measurements over predicts the critical Reynolds number, while the linear stability analysis under predicts it.

These results bring forth the difficulty in experiments and modelling of the effects of fibres on hydrodynamic stability. Where, in this particular case, rheological measurements and simulations fail to quantitatively predict the effect NFC has on the stability of the flow.

Regarding fibres in turbulent boundary layer, more experiments are needed in order to provide data for verification for simulations. The data needed should if possible include velocity data for the fibres and the fluid, as well as rotational velocity and orientation for the fibres.

Due to the inconclusive results from the experiments on the effects of fibres on stability, the need for further studies on this subject is apparent. A study of the orientation of NFC in the channel coupled with the onset of the primary instability would greatly increase the understanding.

CHAPTER 6

Papers & author contributions

Paper 1

Fibre orientation and fibre streaks in turbulent wall bounded flow

M. Kvick (MK), K. Håkansson (KH), F. Lundell (FL), L. Prah Wittberg (LPW) & L. D. Söderberg (DS)

The orientation and spatial distribution of fibres in a turbulent wall bounded flow is studied experimentally. MK and KH performed a majority of the experiments and analysis in close collaboration under supervision of FL, LPW and DS. In addition, KH performed the LDV measurements and MK implemented the anisotropy as an analysis method. MK, KH, FL and LPW wrote the paper jointly with input from DS.

Parts of these results have been published in:

Streak Formation and Fibre Orientation in Near Wall Turbulent Fibre Suspension Flow

M. Kvick, K. Håkansson, F. Lundell, L. D. Söderberg & L. Prah Wittberg

ERCOFTAC bulletin, 2010, Vol. 84

Fibre Streaks in Wall Bounded Turbulent Flow

M. Kvick (MK), K. Håkansson, F. Lundell, L. D. Söderberg & L. Prah Wittberg

7th Int. Conf. on Multiphase Flow

May 30 – June 4 2010, *Tampa, FL, USA*

Paper 2

Measurement of width and streakiness of particle streaks in turbulent flows

K. Håkansson (KH), M. Kvick (MK), F. Lundell (FL), L. Prah Wittberg (LPW) & L. D. Söderberg (DS)

A new method for the quantification of particle streaks is developed. KH and MK developed the method and performed the analysis under supervision of FL,

LPW and DS. KH investigated and accounted for the dependence of concentration, image size, artificial particle size and streak width in the method. MK incorporated the Voronoi method into the analysis. KH, MK, FL and LPW wrote the paper jointly with input from DS.

Paper 3

Effects of nano-fibrillated cellulose on curvature- and rotation-induced instabilities in channel flow

M. Kvick (MK), F. Lundell (FL), L. Prah Wittberg (LPW) & L. D. Söderberg (DS)

The effect of nano-fibrillated cellulose on instability is studied experimentally in a curved rotating channel. MK performed the experiments and analysis under supervision of FL, LPW and DS. MK wrote the paper with input from FL, LPW and DS.

Acknowledgements

The *Wallenberg Wood Science Center* (WWSC) through the *Knut and Alice Wallenberg foundation* is greatly acknowledged for the funding of this work.

I would like to thank my main supervisor Fredrik Lundell, for his great enthusiasm in the world of fibre suspension flows, as well as always being available when a question needed an answer.

Great thanks also to my other supervisors, Daniel Söderberg, who accepted me as a PhD student and introduced me to the world of papermaking and Lisa Prahl Wittberg for the many corrections on various texts and ideas on analysis and interpretation.

Karl Håkansson, who has been collaborating with me on a large part of this thesis, is greatly appreciated for making work interesting and enjoyable, as well as providing an excuse to relax after work, when needed.

A special thanks to Dr. Mihai Mihaescu for comments and suggestions regarding the contents and layout of the thesis.

Prof. Matsubara and Kenta Watanabe are highly appreciated together with the rest of the group at Shinshu University for taking care of me during my visit to Japan.

Thanks to Allan who provided valuable input on the reasoning regarding the fibre orientation and Gabri who showed me how to find my way around the lab.

Thanks to all of you who went out for lunch each day, Karl, Outi, Thomas K, Shintaro. As well as the people who have joined later, Tomas R and Michail.

For the great atmosphere and interesting topics at the coffee breaks in the lab special thanks go to; Bengt, Ylva, Shahab, Sohrab, Renzo, Sissy, Markus, Fredrik, Malte, Olle, Johan, Niklas, Emma, Alexander, Ramin, Alexandre, Afshin, Ramis, Antonio and Ramin.

At OB18 I would like to especially mention Peter, Marit, Stevin, Florian, Johan M, Qiang and Feng.

30 ACKNOWLEDGEMENTS

All the people at WWSC, both in Stockholm and Göteborg are appreciated for enjoyable times at the conferences and doctoral courses.

Finally I would like to acknowledge some people from outside of the academic world, Adam, David, Erik, Ola and Kent for their interest in something I still haven't managed to explained.

Also great thanks to Mamma & Pappa for their support during my studies and for listening to my complaints.

Thank you!

May 2012, Stockholm

Mathias Kvik

References

- ADVANI, S. G. & TUCKER III, C. L. 1987 The use of tensors to describe and predict fiber orientation in short fiber composites. *Journal of Rheology* **31** (8), 751–784.
- AIDUN, C. K., LU, Y. & DING, E. 1998 Direct analysis of particulate suspensions with inertia using the discrete boltzmann equation. *Journal of Fluid Mechanics* **373**, 287–311.
- ANDERSSON, H. I., ZHAO, L. & BARRI, M. 2012 Torque-coupling and particleturbulence interactions. *Journal of Fluid Mechanics* **696**, 319–329.
- AZAIÉZ, J. 2000 Linear stability of free shear flows of fibre suspensions. *Journal of Fluid Mechanics* **404**, 179–209.
- BATCHELOR, G. K. 1970*a* Slender-body theory for particles of arbitrary cross-section in stokes flow. *Journal of Fluid Mechanics* **44** (03), 419–440.
- BATCHELOR, G. K. 1970*b* The stress system in a suspension of force-free particles. *Journal of Fluid Mechanics* **41** (03), 545–570.
- BATCHELOR, G. K. 1971 The stress generated in a non-dilute suspension of elongated particles by pure straining motion. *Journal of Fluid Mechanics* **46** (04), 813–829.
- BRETHERTON, F. P. 1962 The motion of rigid particles in a shear flow at low reynolds number. *Journal of Fluid Mechanics* **14** (02), 284–304.
- CARLSSON, A. 2009 Near wall fibre orientation in flowing suspensions. PhD thesis, KTH Mechanics, Royal Institute of Technology.
- CARLSSON, A., HÅKANSSON, K., KVICK, M., LUNDELL, F. & SÖDERBERG, L. D. 2011 Evaluation of steerable filter for detection of fibers in flowing suspensions. *Experiments in Fluids* **51**, 987–996.
- CARLSSON, A., LUNDELL, F. & SÖDERBERG, L. D. 2007 Fiber orientation control related to papermaking. *Journal Fluids Engineering* **129** (4), 457–465.
- COX, H. L. 1952 The elasticity and strength of paper and other fibrous materials. *British Journal of Applied Physics* **3** (3), 72.
- CROWE, C., SOMMERFELD, M. & TSUJI, Y. 1998 *Multiphase flows with particles and droplets*. CRC Press.
- DERAKHSHANDEH, B., KEREKES, R., HATZIKIRIAKOS, S. & BENNINGTON, C. 2011 Rheology of pulp fibre suspensions: A critical review. *Chemical Engineering Science* **66** (15), 3460 – 3470.

- GOLDSMITH, H. & MASON, S. 1962 The flow of suspensions through tubes. I. single spheres, rods, and discs. *Journal of Colloid Science* **17** (5), 448 – 476.
- GUPTA, V. K., SURESHKUMAR, R., KHOMAMI, B. & AZAIEZ, J. 2002 Centrifugal instability of semidilute non-brownian fiber suspensions. *Physics of Fluids* **14** (6), 1958–1971.
- HÅKANSSON, K., KVICK, M., LUNDELL, F., PRAHL WITTEBERG, L. & SÖDERBERG, L. D. 2012 Measurement of width and amplitude of particle streaks in turbulent flows. To be submitted.
- HARRIS, J. B. & PITTMAN, J. F. T. 1975 Equivalent ellipsoidal axis ratios of slender rod-like particles. *Journal of Colloid and Interface Science* **50** (2), 280 – 282.
- JEFFERY, G. B. 1922 The motion of ellipsoidal particles immersed in a viscous fluid. *Proceedings of the Royal Society of London. Series A, Containing Papers of a Mathematical and Physical Character* **102** (715), pp. 161–179.
- KAREMA, H., KATAJA, M., KELLOMKI, M., SALMELA, J. & SELENIUS, P. 1999 Transient fluidisation of fibre suspension in straight channel flow. *International Paper Physics Conference Proceedings* .
- KVICK, M., HÅKANSSON, K., LUNDELL, F., PRAHL WITTEBERG, L. & SÖDERBERG, L. D. 2012a Fibre orientation and fibre streaks in turbulent wall bounded flow. To be submitted.
- KVICK, M., LUNDELL, F., PRAHL WITTEBERG, L. & SÖDERBERG, L. D. 2012b Effects of nano-fibrillated cellulose on curvature- and rotation-induced instabilities in channel flow. Manuscript in preparation.
- LUNDELL, F. & CARLSSON, A. 2010 Heavy ellipsoids in creeping shear flow: Transitions of the particle rotation rate and orbit shape. *Physical Review E* **81**, 016323.
- MARCHIOLI, C., FANTONI, M. & SOLDATI, A. 2010 Orientation, distribution, and deposition of elongated, inertial fibers in turbulent channel flow. *Physics of Fluids* **22** (3), 033301.
- MATSSON, O. J. E. & ALFREDSSON, P. H. 1990 Curvature- and rotation-induced instabilities in channel flow. *Journal of Fluid Mechanics* **210**, 537–563.
- MORTENSEN, P., ANDERSSON, H., GILLISSEN, J. & BOERSMA, B. 2008 On the orientation of ellipsoidal particles in a turbulent shear flow. *International Journal of Multiphase Flow* **34** (7), 678 – 683.
- NORMAN, B. A. 2005 *The Ljungberg Textbook - Paper Processes*. Fibre and Polymer Technology, KTH.
- NSOM, B. 1996 Stability of fiber suspension flow in curved channel. *Journal de Physique II* **6** (10), 1483–1492.
- PETRIE, C. J. 1999 The rheology of fibre suspensions. *Journal of Non-Newtonian Fluid Mechanics* **87** (2-3), 369 – 402.
- PILIPENKO, V. N., KALINICHENKO, N. M. & LEMAK, A. S. 1981 Stability of the flow of a fiber suspension in the gap between coaxial cylinders. *Soviet Physics Doklady* **26**, 646.
- POPE, S. B. 2000 *Turbulent flows*. Cambridge University Press.
- SUBRAMANIAN, G. & KOCH, D. L. 2006 Inertial effects on the orientation of nearly spherical particles in simple shear flow. *Journal of Fluid Mechanics* **557**, 257–296.

- TOMS, B. A. 1948 Some observations on the flow of linear polymer solutions through straight tubes at large reynolds numbers. In *Proceedings of the First International Congress on Rheology*, , vol. 2, pp. 135–141. North Holland Publication Company.
- TREVELYAN, B. & MASON, S. 1951 Particle motions in sheared suspensions. I. rotations. *Journal of Colloid Science* **6** (4), 354 – 367.
- VASELESKI, R. C. & METZNER, A. B. 1974 Drag reduction in the turbulent flow of fiber suspensions. *AIChE Journal* **20** (2), 301–306.
- VIRK, P. S. 1975 Drag reduction fundamentals. *AIChE Journal* **21** (4), 625–656.
- VIRK, P. S., MERRILL, E. W., MICKLEY, H. S., SMITH, K. A. & MOLLO-CHRISTENSEN, E. L. 1967 The toms phenomenon: turbulent pipe flow of dilute polymer solutions. *Journal of Fluid Mechanics* **30** (02), 305–328.
- WHITE, C., SOMANDEPALLI, V. & MUNGAL, M. 2004 The turbulence structure of drag-reduced boundary layer flow. *Experiments in Fluids* **36**, 62–69.
- ZACKSENHOUSE, M., ABRAMOVICH, G. & HETSRONI, G. 2001 Automatic spatial characterization of low-speed streaks from thermal images. *Experiments in Fluids* **31** (2), 229–239.
- ZHANG, H., AHMADI, G., FAN, F.-G. & MCLAUGHLIN, J. B. 2001 Ellipsoidal particles transport and deposition in turbulent channel flows. *International Journal of Multiphase Flow* **27** (6), 971 – 1009.
- ZHAO, L. H., ANDERSSON, H. I. & GILLISSEN, J. J. J. 2010 Turbulence modulation and drag reduction by spherical particles. *Physics of Fluids* **22** (8), 081702.
- ZHENJIANG, Y., JIANZHONG, L. & ZHAOSHENG, Y. 2004 Hydrodynamic instability of fiber suspensions in channel flows. *Fluid Dynamics Research* **34** (4), 251 – 271.

Part II

Papers

Paper 1

Fibre orientation and fibre streaks in turbulent wall bounded flow

By Mathias Kvick^{1,2}, Karl Håkansson^{1,2}, Fredrik Lundell^{1,2},
Lisa Prahl Wittberg^{1,2} & L. Daniel Söderberg^{1,3}

¹ Wallenberg Wood Science Center, KTH Mechanics, Royal Institute of Technology, SE – 100 44, Stockholm, Sweden

² Linné Flow Centre, KTH Mechanics, Royal Institute of Technology, SE – 100 44, Stockholm, Sweden

³ Innventia AB, BOX 5604, SE-114 86, Stockholm, Sweden

To be submitted

The behaviour of fibres in a wall bounded turbulent shear flow is investigated. Understanding and modelling of fiber suspension flow is necessary for improvements in many applications, e.g. papermaking. Experimental data covering wide parameter spaces is an important ingredient in this effort. A dilute fibre suspension flowing down an inclined glass plate is studied. Images of the fibres in the flow are acquired from beneath the glass plate and the images are analysed using a steerable filter, providing the position and orientation of the fibres. Both fibre orientation distributions and spatial distributions are investigated. It is found that the length of the fibres plays an important role in the overall fibre orientation distribution. The flow conditions are also observed to have an effect on the orientation on the shorter fibres. A small amount of polymers added to the suspension is found to have an impact on the fibre orientation. Furthermore, the results indicate that increased fibre concentration drives the fibres towards a particular orientation, indicating that fibre interactions cannot be modelled as a solely diffusive effect in this case. Moreover, the fibres are found to form streamwise streaks of different intensity. The width of these streaks are measured and corresponds to the same width as the low velocity streaks found in turbulent wall layers. The intensity of the fibre streaks are found to vary with the flow conditions.

1. Introduction

When producing paper, the mass and orientation distribution of cellulose fibres, and therefore also the mechanical properties of the paper are highly dependent on the flow in the headbox nozzle, Cox (1952), Lundell *et al.* (2011). The headbox is a 2D contraction generating a thin, wide fibre suspension sheet that

is jetted out onto permeable forming wires, where the paper is formed. The flow in the headbox is highly complex, being both turbulent and extensional as well as having walls and vanes present. Increasing the knowledge of the behaviour of fibres in turbulent wall bounded flows will provide better understanding of the effects the headbox has on the final paper. Not only the distribution of the fibre orientations, i.e. their individual direction in the flow, but also the overall fibre orientation and the distribution of the fibres in the cross direction (spanwise) is of interest.

Carlsson *et al.* (2007) and Carlsson (2009) studied a laminar half channel flow with a dilute fibre suspension. The focus was mainly on fibre orientation and fibre location in the wall normal direction. The fibres had a density greater than that of the liquid phase. It was concluded that most fibres with small aspect ratio were located closer than half of a fibre length from the wall and aligned perpendicular to the flow. On the other hand, fibres with greater aspect ratios were found to be located at distances more than half a fibre length away from the wall and oriented in the flow direction. It was suggested that this behaviour occurred due to a competition between fluid inertia (driving the fibres towards the flow direction) and the combination of sedimentation and wall contacts (driving the fibres away from the flow direction).

Particle streaks have been observed both in experiments and simulations of spherical particles in turbulent channel flow (e.g. Kaftori *et al.* (1995a), Kaftori *et al.* (1995b), Ninto & Garcia (1996), Marchioli & Soldati (2002) and Narayanan *et al.* (2003)). Marchioli & Soldati (2002) concluded that the largest preferential concentration occurs close to the wall, and the particles accumulate in the low speed velocity streaks.

Zhang *et al.* (2001), Mortensen *et al.* (2008) and Marchioli *et al.* (2010) performed DNS (Direct Numerical Simulation) of fibre suspensions in turbulent channel flow. Zhang *et al.* (2001) studied the transport and deposition of fibres while Mortensen *et al.* (2008) as well as Marchioli *et al.* (2010) investigated the effects of aspect ratio and response time on the orientation of the fibres. In all the above mentioned studies the non-spherical particles also accumulated in the low velocity streaks and the fibres tended to align in the flow direction with increasing aspect ratio.

In this study, the orientation and accumulation of fibres in turbulent half channel flow is investigated experimentally. Quantified data is obtained and discussed. The results provide several distinct observations that can be used for development and verification of numerical models. In section 2 the experimental setup and the methods used to extract data is explained. The results are presented in sections 3 and 4, focussing on fibre orientation as well as the effect of polymers and investigating streamwise streaks of high local fibre concentration. In section 5 the results are discussed and the conclusions are summarised in section 6.

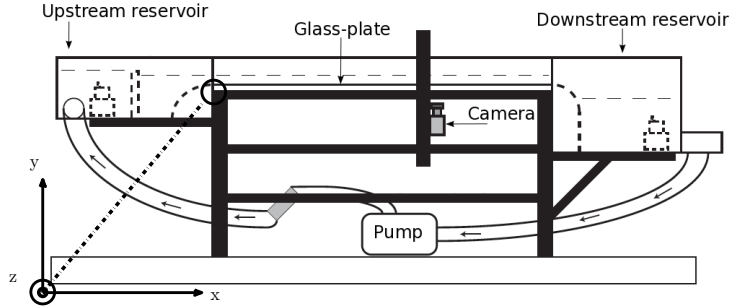


FIGURE 1. Schematic of the water-table, camera and pumps. The length of the glass plate is approximately 2 m and the width 0.6 m.

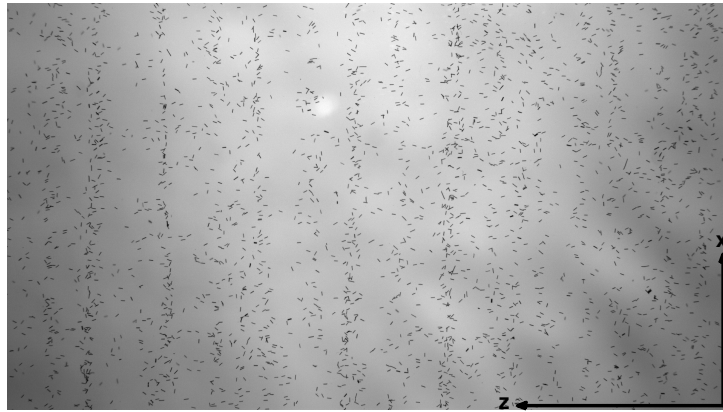


FIGURE 2. Typical image of the fibre suspension acquired during experiment. The flow is in positive x -direction. The black dyed fibres can clearly be seen in the flow. The dimensions of the image is $\Delta x = 5$ cm and $\Delta z = 10$ cm.

2. Methods

2.1. Flow apparatus and image acquisition

The experimental setup consisted of a water-table and a camera, shown in figure 1. The water-table was filled with a dilute suspension of fibres and water. The suspension was pumped from a downstream reservoir to an upstream reservoir and was free to flow down an inclined glass plate to the downstream reservoir. Submersible pumps were placed in the upstream and downstream reservoirs stirring the suspension and preventing fibres from sedimenting there.

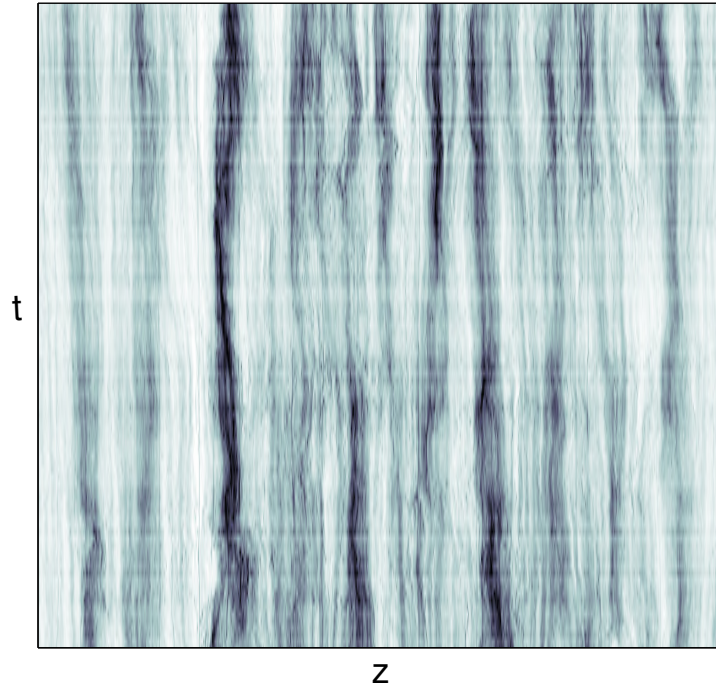


FIGURE 3. Visualisation of fibre streaks in time, where each row corresponds to an image such as figure 2 summed in the streamwise direction, $\Delta z = 10$ cm and total time lapse $\Delta t = 7.7$ s.

Underneath the glass plate, at a downstream position, a camera was placed in order to acquire images of the fibres in the flowing suspension. A stroboscope was mounted close to the camera and produced short flashes in order to generate sharp images. The depth of field of the camera lens was enough to detect all fibres in the water layer in all experiments regardless of the fibres wall normal position. However, at the acquisition position, located 1100 mm downstream of the inlet of the glass plate, most fibres were observed to have sedimented and be located in the direct proximity of the wall. A typical image of the suspension is shown in figure 2, corresponding to the x - z plane, where x, y, z are the flow, wall normal and spanwise directions, respectively. The origin is positioned on the leading edge of the glass plate with $z = 0$ on its centreline. In each experiment, 150 images were acquired and in each image 200 – 3000 fibres were detected, ensuring converging statistics. In most experiments, fibres could be seen to gather in streamwise streaks, a visualisation of these fibre streaks is displayed in figure 3. This figure is based on 96 images captured during 7.7 s;

each image is summed in the streamwise direction and is a row in the final figure.

The flow down the glass plate was driven by gravity alone, and thus the wall shear stress, τ_w , can be calculated through a force balance between the glass plate and the water layer (e.g. Acheson (1990));

$$\tau_w = \rho g h \sin \alpha. \quad (1)$$

Here ρ is the density of water, g is the gravitational acceleration, h is the height of the water layer and α is the inclination angle of the glass plate. The flow can be seen as an approximation of a half-channel flow, since the velocity gradient is zero on the centreline of a full channel (with height $2h$). Due to the large viscosity difference between water and air the conditions on the free surface in the present setup are very close to this condition.

In a channel flow, the friction Reynolds number is defined as;

$$Re_\tau = \frac{h}{\nu} u_\tau = \frac{h}{\nu} \sqrt{\frac{\tau_w}{\rho}} = \frac{h \sqrt{g h \sin \alpha}}{\nu}, \quad (2)$$

where $u_\tau = \sqrt{\tau_w/\rho}$ is the friction velocity and ν is the kinematic viscosity. Note that Re_τ is only dependent on material properties and the geometry of the channel. The effects of fluid and particle inertia on particle rotation (for a given density ratio) is quantified by a particle Reynolds number Re_p defined as (Aidun *et al.* 1998);

$$Re_p = \dot{\gamma} \frac{l_f^2}{\nu} = \frac{\tau_w l_f^2}{\rho \nu} = \frac{l_f^2 g h \sin \alpha}{\nu^2}, \quad (3)$$

where $\dot{\gamma}$ represents the shear rate at the glass plate and l_f is the fibre length. As defined here, Re_p characterises the hydrodynamic torques acting on the particles in the flow. The actual water layer thickness, h , is 8–12 mm depending on parameter combination.

Rigid cellulose acetate fibres with a density of $\rho_f = 1300 \text{ kg/m}^3$ and aspect ratios $r_p = 7, 14$ and 28 , corresponding to fibre lengths $l_f = 0.5, 1$ and 2 mm and cross section $70 \text{ }\mu\text{m}$, were mixed with 120 l of water, resulting in low concentration suspensions ($0.00042 - 0.0033\%$ by weight, corresponding to a number density of $nl^3 = 0.0008 - 0.0066$). However, due to sedimentation, most fibres were located close to the wall, resulting in higher local concentration. The local concentration was calculated via the number of fibres in each image. For one flow case, the effect of concentration was studied using concentrations up to $nl^3 = 0.031$. Only mono dispersed suspensions were studied.

The setup was limited to $Re_\tau \leq 210$, due to the generation of surface waves at higher Reynolds numbers.

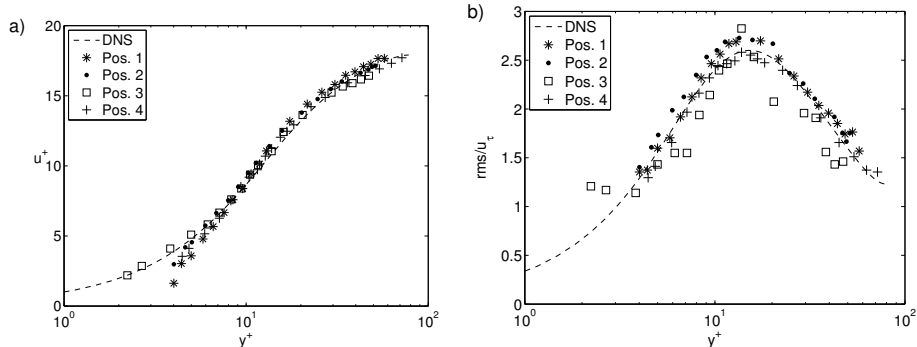


FIGURE 4. Velocity statistics measured by LDV at $(x, z) = (1100, 0)$ mm, $(1100, \pm 200)$ mm and $(800, 0)$ mm, positions 1, 2, 3 and 4, respectively, at $Re_\tau = 88$. The experimental data is compared to DNS-data from a full channel flow at $Re_\tau = 80$. (a) Mean velocity profiles. (b) Velocity fluctuations.

2.2. Laser doppler velocimetry

In order to ensure that the flow is fully developed and homogenous, Laser Doppler Velocimetry (LDV) measurements without fibres were carried out at $(x, z) = (1100, 0)$ mm, $(1100, \pm 200)$ mm and $(800, 0)$ mm. Streamwise velocity and *rms* profiles for $Re_\tau = 88$ are displayed in figure 4, where the dashed lines are comparisons with DNS for a full channel flow at $Re_\tau = 80$ (Tsukahara *et al.* 2005). The agreement between the experiment and DNS is good. The velocities are normalized with u_τ and the vertical coordinate with the viscous length scale $l^+ = \nu/u_\tau$.

2.3. Fibre detection and streak analysis

The images were processed by first subtracting the background noise. The fibres position (x - and z -coordinate in the image), and the orientation angle β (measured as positive rotation around the y -axis where $\beta = 0$ is the flow direction) were obtained using a second order ridge detector within the class of steerable filters, Jacob & Unser (2004). The filter has earlier been evaluated by Carlsson *et al.* (2011), reporting the effect of noise and unsharpness of the images on the orientation angle to be less than 1° for moderate levels of disturbances.

In order to analyse the accumulation of fibres into streamwise streaks, observed in the experiments, the method described in Håkansson *et al.* (2012) was applied. In short, the fibre positions are used to create an image with artificial fibres where the orientation and size of the fibres are identical. The new image is summed in the streamwise direction. The resulting signal is

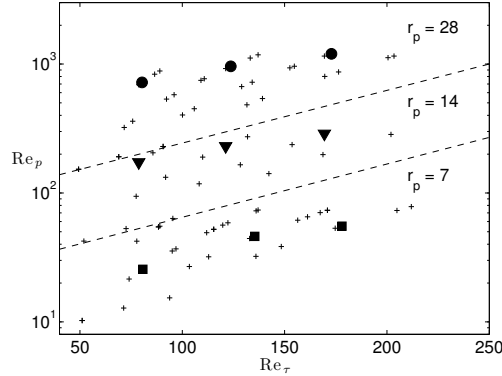


FIGURE 5. Parameter combinations studied, (+) indicate all measurements made. Measurements marked with the symbols (●, ▼, ■) corresponds to the data shown in figure 6. At each marked position, 150 images have been acquired and analysed. Three distinct regions are shown in which the aspect ratio is constant.

correlated with itself, which, when performed for a whole set of images, results in a mean streak width and a mean streakiness of the fibre structure. In the analysis, great care is taken to compensate for the influence of concentration, image size, fibre size and streak width.

3. Fibre orientation results

In figure 5, the parameter combinations at which measurements have been performed are shown. The friction Reynolds number, Re_τ , was varied between 50 and 210, and the particle Reynolds number, Re_p between 10 and 10^3 . Note that the parameter space can be divided into three regions, without overlap, where each region corresponds to one of the three aspect ratios.

In the following sections the effect of aspect ratio, Re_τ , downstream position and concentration on the fibre orientation will be investigated. The effect on fibre orientation of small amount of polymers in the suspension is also studied. Fibre orientation and anisotropy data will be presented.

3.1. Anisotropy

In order to quantify the anisotropy of the fibre orientation distribution, a unit vector \mathbf{p} is associated with each fibre, Advani & Tucker III (1987). The components of \mathbf{p} are directly related to the orientation of the fibre. In this case, since the acquired orientation is 2 - dimensional, only one orientation angle, β ,

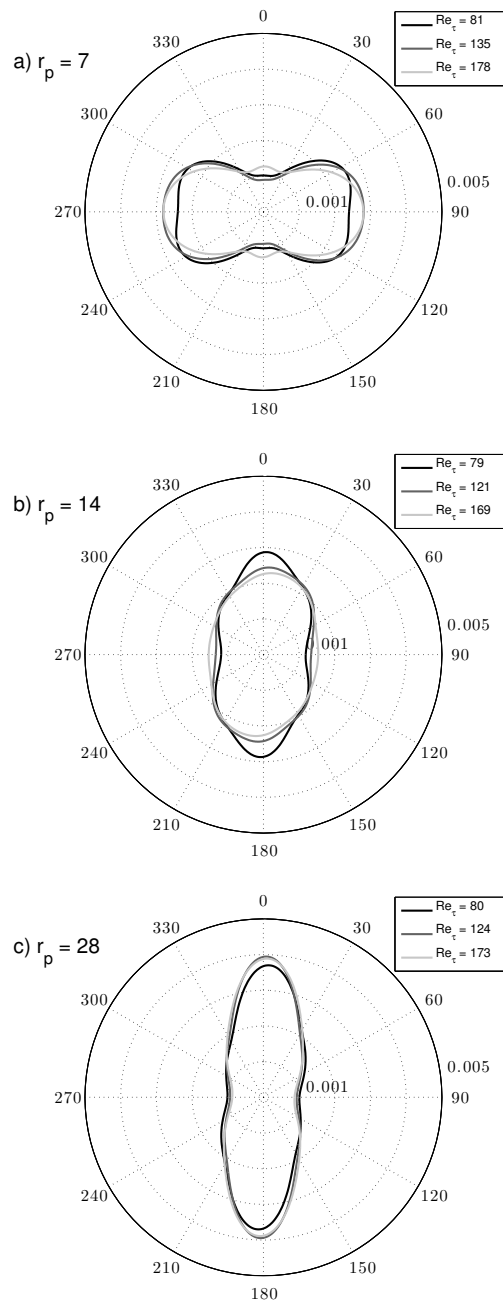


FIGURE 6. Fibre orientation distributions for (a) $r_p = 7$, (b) $r_p = 14$ and (c) $r_p = 28$, at positions in the parameter space marked with $(\bullet, \blacktriangledown, \blacksquare)$ in figure 5.

is used.

$$\begin{aligned} p_1 &= \int_0^\pi \cos \beta \, d\beta \\ p_2 &= \int_0^\pi \sin \beta \, d\beta \end{aligned} \quad (4)$$

The components of the second order orientation tensor \mathbf{a}_2 in which $a_{ij} = p_i p_j$ are now defined as;

$$\begin{aligned} a_{11} &= \int_0^\pi \cos^2 \beta \, d\beta \\ a_{12} &= a_{21} = \int_0^\pi \cos \beta \sin \beta \, d\beta \\ a_{22} &= \int_0^\pi \sin^2 \beta \, d\beta \end{aligned} \quad (5)$$

The anisotropy is then obtained as follows;

$$A = a_{11}/a_{22}.$$

3.2. Orientation distributions and effect of aspect ratio

In figures 6a–6c, fibre orientation distributions for the different aspect ratios at similar friction Reynolds numbers are displayed. The orientation angle, β , is defined to be zero, ($\beta = 0$), in the streamwise direction, and $\beta = 90$ in the spanwise direction. It is evident from the figures that the aspect ratio plays an important role for the fibre orientation distribution. In figure 6a, showing the fibre orientation distribution for the shortest fibres (aspect ratio $r_p = 7$), most of the fibres are located between 45 and 135 degrees, as well as between 225 and 315 degrees since the distribution is symmetric. A large difference is found if comparing with figure 6c, in which the fibre orientation distribution for fibres with aspect ratio $r_p = 28$ is shown, where most fibres have an orientation close to $\beta = 0^\circ$, *i.e.* the streamwise direction.

As shown in figure 7, the fibres with aspect ratios $r_p = 28$, (\bullet) and $r_p = 7$, (\blacksquare), are oriented ($A = 2$ and 0.5 , respectively), while the medium length fibres, $r_p = 14$, (\blacktriangledown) are more isotropic. This information is also possible to visually extract from the fibre orientation distributions in figure 6.

3.2a. *Effect of Re_τ .* In figure 7, the anisotropy for all measurements are shown versus the friction Reynolds number. For the longer fibres, with aspect ratio $r_p = 28$, (\bullet), A shows no distinct trend. For fibres with $r_p = 14$, (\blacktriangledown), A decreases with a near constant slope. For the shortest fibres, $r_p = 7$, (\blacksquare), A first decreases, assumes a minimum at $Re_\tau \approx 110$, and thereafter increases with increasing Re_τ . For the two shorter fibres, the anisotropy A approaches 1, as Re_τ increases, indicating an approach to isotropy. The open symbols in figure 7 refer to concentration variations and will be discussed later.

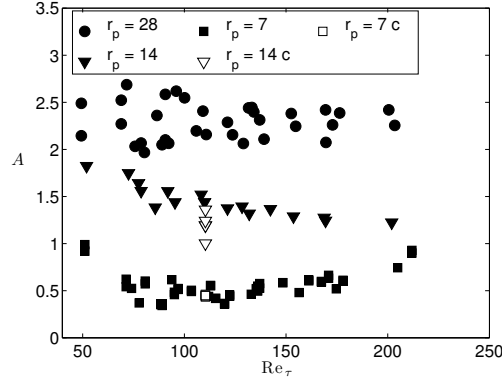


FIGURE 7. Anisotropy for all measurements versus Re_τ , where (●, ▼, ■) represents $r_p = 28$, $r_p = 14$ and $r_p = 7$, respectively and ▽, □ represents measurements where only the concentration of fibres have been altered, the exact concentrations can be found in figure 9c.

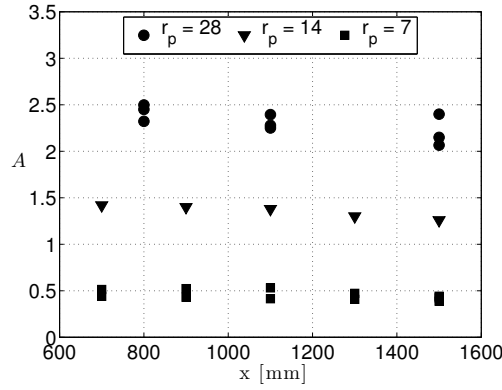


FIGURE 8. Anisotropy as a function of streamwise position; (●) for $r_p = 28$, (▼) for $r_p = 14$ and (■) for $r_p = 7$, where the downstream position has been changed for each aspect ratio. $Re_\tau = 100 - 200$ and $Re_p = 200 - 1100$. The acquisition point used for all other measurements are located at 1100 mm downstream from the beginning of the glass plate.

3.2b. *Effect of downstream position.* The anisotropy at several streamwise positions is plotted in figure 8. The measurements have been performed with different fibre lengths as well as for different friction Reynolds numbers, ranging from 100 to 200. All fibre lengths have a slight decrease in anisotropy as

the fibres progress downstream, indicating that the fibre orientation distributions are not fully developed at the acquisition point. However, the change in anisotropy is slow, implying that the major changes in orientation has occurred further upstream.

3.2c. *Effect of number of fibres.* Since the local concentration reached in the experiments is believed to fall into the semi-dilute regime, experiments were performed for constant flow conditions and varied concentrations. In figure 9, results of fibre orientation from experiments with different fibre concentration is displayed; (a) and (b) as well as the open symbols in (c) show data from $Re_\tau = 110$ and constant Re_p for each aspect ratio whereas the filled symbols are all the cases shown in figure 5. The concentration variations from $Re_\tau = 110$ are also shown with open symbols in figure 7.

Here the local concentration is computed from the mean number of fibres found in each set of images. Figure 9a and 9b shows the orientation distributions for fibres with $r_p = 7$ and $r_p = 14$ respectively, and in figure 9c, the anisotropy is plotted. The squares (open and closed) in figure 9c implies that the local concentration has no impact on the shorter fibres, whereas for the intermediate fibres ($\blacktriangledown, \triangledown$) A increases from close to unity with increasing concentration. The post processing fibre detection algorithm was limiting the experiment in terms of studying greater concentrations. The orientation distributions are not longer constant at $nl^3 > 0.01$, indicating that the suspension no longer is dilute.

3.2d. *Effect of polymers.* The addition of polymers to the suspension is interesting from an orientation control point of view. Therefore experiments with a small addition (40ppm) of Poly-Ethylene-Oxide (PEO) were performed. Viscosity measurements of the fluid phase with a rotational viscometer were performed in order to ensure that the shear viscosity was not changed as compared to water. Fibres with aspect ratios 7 and 14 where used at different friction Reynolds numbers, the results are shown in figure 10. The anisotropy is not notably changed for $r_p = 7$. However, for $r_p = 14$, all measurements have a lower anisotropy compared to the case where the fluid phase is water. Polymers have in previous studies, White *et al.* (2004), been shown to interact with and to modify the quasi streamwise streaks in a turbulent wall bounded flow. Furthermore, White *et al.* (2004) found that the addition of polymers had an effect on the buffer layer, which could be the reason for the results displayed in figure 10. Since the length of the fibres with aspect ratio 14 ($l_f = 6l^+ - 18l^+$) corresponds to the location of the buffer layer, while the shorter fibres with aspect ratio 7 have a length ($l_f = 3l^+ - 9l^+$) that is close to the height of the viscous sublayer.

3.2e. *Orientation in streaks.* In order to investigate whether fibres inside streaks are oriented differently as compared to fibres not located in streaks, the 10%

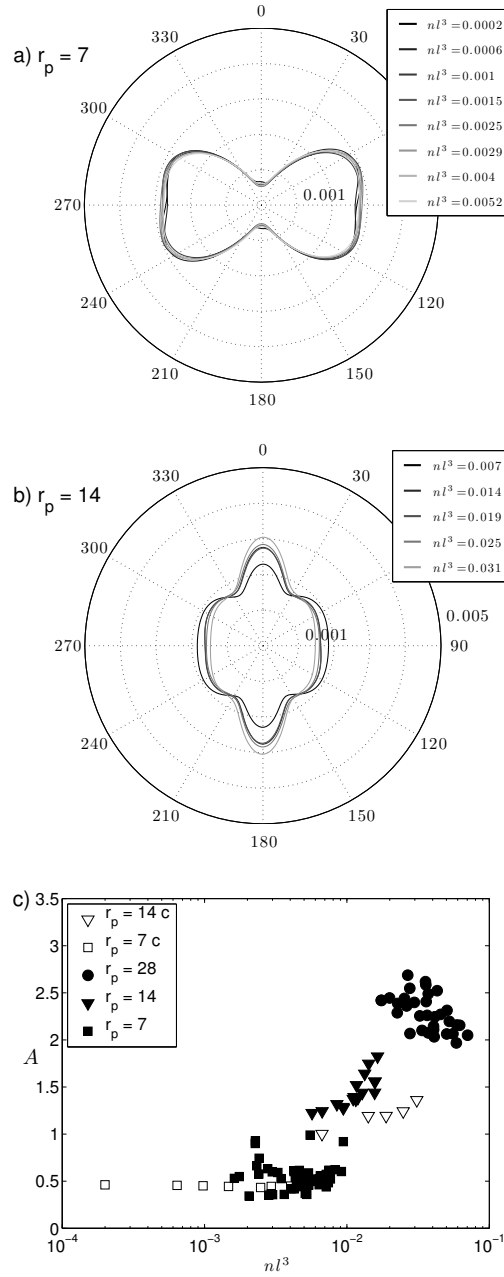


FIGURE 9. Orientation distributions of fibres with (a) $r_p = 7$ and (b) $r_p = 14$, where the concentration has been changed for each aspect ratio. $Re_\tau = 110$. c) Anisotropy quotient versus nl^3 , where open symbols (\square and ∇) represents the measurements in (a) and (b) where the flow conditions have been kept constant, the filled symbols (\bullet , \blacktriangledown , \blacksquare) represents all measurements performed, including different Re_τ .

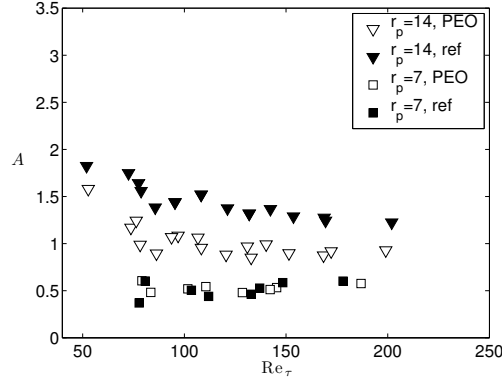


FIGURE 10. Anisotropy for suspension containing PEO (∇ and \square) compared to the reference (\blacktriangledown and \blacksquare) where the fluid phase is tap water.

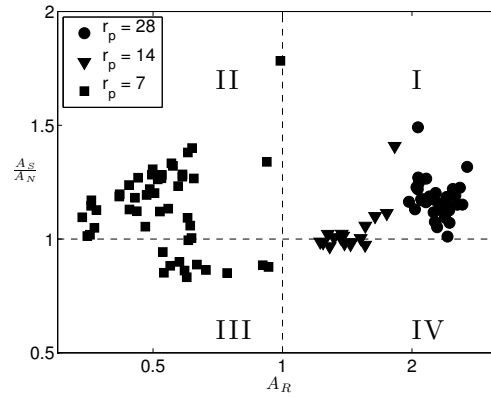


FIGURE 11. Quota of the anisotropy for fibres inside, A_S , and outside, A_N , of streaks compared with the reference anisotropy, A_R , for all cases.

most clustered (from Voronoi analysis) fibres in each image are defined to be in streaks, and the 10% least clustered are considered to be located outside the streaks. Figure 11 shows the anisotropy in streaks, A_S , normalised with anisotropy of the fibres that are not in streaks, A_N , as function of the original (reference) anisotropy of all fibres in the measurement. The results in this plot belong to one of four quadrants I-IV. Data points in quadrants I and III means that the fibres in the streaks have a preferred orientation (in the flow direction in I and normal to the flow in III) compared to the fibres outside streaks. Data points in quadrants II and IV, on the other hand, means that the fibres in the

streaks have a more random orientation than the fibres outside of the streaks. The main observation from figure 11 is that for the cases with high A_R the fibres in the streaks tend to be even more aligned than the fibres outside the streaks. (compare quadrant I and IV).

4. Streakiness and fibre streak width results

In most experiments, the fibres accumulated in long streamwise streaks.

In figure 12a, the relative streakiness, Ξ , is shown as a function of Re_τ . The larger the dot, the stronger the tendency for the fibres to accumulate into streamwise streaks. The measurements marked with a (\times) could not be evaluated due to too low (streakiness analysis) or too high (fibre detection) fibre concentration. Moreover, the streakiness displays a maximum at $Re_\tau \approx 110$ as is shown in figure 12b, where the relative streakiness is depicted as function of Re_τ .

In figure 12c the width of the fibre streaks are compared with the value $50l^+$ (full line), an empirical value of the streak width of the low velocity streaks, e.g. Zacksenhouse *et al.* (2001). The dashed line represents $70l^+$ and figure 12c shows that most experimental streak widths fall in between these two line. The fibre streaks scale in the same manner as low velocity streaks in a flow without fibres, although slightly wider. Similar behaviour has been reported for spherical particles in channel flows where the spheres has been observed to widen the velocity streaks, Zhao *et al.* (2010).

5. Discussion

The results show a major impact of fibre aspect ratio on the orientation of the fibres as they have sedimented to the wall region. In comparison with the major impact of fibre aspect ratio, effects such as Reynolds number, concentration and addition of 40 ppm PEO are of secondary importance. These factors only modify the fibre orientation slightly. The orientation behaviour is such that shorter fibres ($r_p = 7$) are oriented normal to the flow direction whereas long fibres ($r_p = 28$) are oriented in the flow direction. The intermediate fibres ($r_p = 14$) give more isotropic orientation distributions.

This orientational behaviour is similar to the one observed in experiments on fibre orientation in laminar flow by Carlsson *et al.* (2007), Carlsson (2009). In the laminar case, a combined theoretical/numerical study showed that the difference in orientational behaviour between short and long fibres occurred due to a competition between the effects of sedimentation towards the wall and direct wall interaction (driving the fibres towards an orientation normal to the flow) and the effects of fluid inertia (when leaving the Stokes flow limit) counteracting this tendency.

In the present work, the turbulent case studied also contain particle inertia, turbulent fluctuations as well as particle interaction. The fact that the laminar

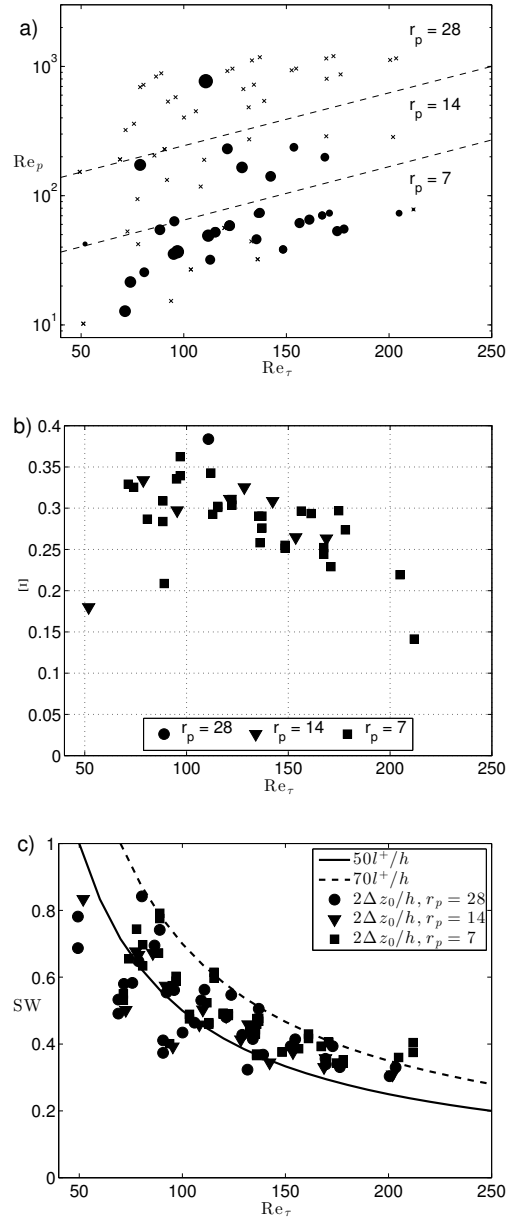


FIGURE 12. (a) Streakiness, bigger dots represent a higher degree of streakiness; (x) represents measurements where streakiness data could not be determined due to insufficient or excessive fibre concentration. (b) Relative streakiness, Ξ , as function of Re_τ , higher value represents higher streakiness. (c) streak widths normalised with the height of the waterlayer for $r_p = 28$ (\bullet), $r_p = 14$ (\blacktriangledown), $r_p = 7$ (\blacksquare), $50 l^+/h$ (full line) and $70 l^+/h$ (dashed line).

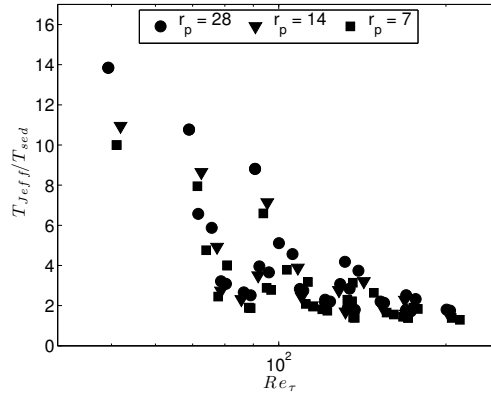


FIGURE 13. The ratio of the Jeffrey period and the sedimentation time from half a fibre length versus the friction Reynolds number.

and turbulent case are fairly similar shows that a detailed modelling of the physics of the hydrodynamic and direct interaction with the wall together with particle and fluid inertia are important. Once such models are at hand, the effect of different components of this complex system can be evaluated. It is possible that the similarity between the laminar and the turbulent results are a coincidence and that the present observations are a results of fibre interaction with the turbulence.

Thus, even though the number of Jeffrey periods, Jeffrey (1922), performed by the fibres during the time at which they interact directly with the wall is fairly low (see figure 13), the interactions with the wall are probably critical.

Two final points will be made that are both related to the concept of diffusivity. The present results indicate that the orientation of the fibres is governed by mean shear and wall interactions, even though the turbulence have a clear impact on organising the fibres into streaks. It should also be noted that the only distinct effect of concentration was an *increase* in anisotropy with increasing concentration, showing that the fibre interaction cannot be modelled as diffuse effects on the orientation distribution. Instead, the results indicate that increased fibre concentration drives the fibres towards a particular orientation (in our case an alignment in the flow direction).

6. Conclusions

Orientation and distribution of fibres in turbulent flow in the neighbourhood of a solid wall has been studied. The flow regime studied is $50 < Re_{\tau} < 210$. The main conclusions are

- The fibre orientation depends on the fibre length normal to the flow for $r_p = 7$ and aligned with the flow for $r_p = 28$.
- The intermediate fibres ($r_p = 14$), displayed a more isotropic orientation distributions.
- For the intermediate fibres, the orientation distribution varied with concentration. At higher concentration, the fibre orientation was more anisotropic.
- A polymer (PEO) concentration of 40 ppm made the orientation distribution of the intermediate fibres more isotropic. The shorter fibres were not affected.
- The fibres organise themselves in streaks. The streakiness vary with Reynolds number and show a maximum around $Re_\tau = 110$.
- The results indicate that fibre interactions cannot be modelled as a diffuse effect on the orientation.

Acknowledgements

Thanks to Dr. Allan Carlsson for providing valuable input during the experiment and analysis. Mr Joseph Fjellgren is acknowledged for the schematic drawing of the setup. This work was funded by the Wallenberg Foundation, through the Wallenberg Wood Science Center. Dr. Lundell and Dr. Prahla Wittberg has also been funded by the Swedish Research Council, VR.

References

- ACHESON, D. J. 1990 *Elementary Fluid Dynamics*. Oxford University Press.
- ADVANI, S. G. & TUCKER III, C. L. 1987 The use of tensors to describe and predict fiber orientation in short fiber composites. *Journal of Rheology* **31** (8), 751–784.
- AIDUN, C. K., LU, Y. & DING, E. 1998 Direct analysis of particulate suspensions with inertia using the discrete boltzmann equation. *Journal of Fluid Mechanics* **373**, 287–311.
- CARLSSON, A. 2009 Near wall fibre orientation in flowing suspensions. PhD thesis, KTH Mechanics, Royal Institute of Technology.
- CARLSSON, A., HÅKANSSON, K., KVICK, M., LUNDELL, F. & SÖDERBERG, L. D. 2011 Evaluation of steerable filter for detection of fibers in flowing suspensions. *Experiments in Fluids* **51**, 987–996.
- CARLSSON, A., LUNDELL, F. & SÖDERBERG, L. D. 2007 Fiber orientation control related to papermaking. *J. Fluids Eng.* **129** (4), 457–465.
- COX, H. L. 1952 The elasticity and strength of paper and other fibrous materials. *British Journal of Applied Physics* **3** (3), 72.
- HÅKANSSON, K., KVICK, M., LUNDELL, F., PRAHL-WITTEBERG, L. & SÖDERBERG, L. D. 2012 Measurement of width and amplitude of particle streaks in turbulent flows. Submitted to Experiments in Fluids.
- JACOB, M. & UNSER, M. 2004 Design of steerable filters for feature detection using canny-like criteria. *Pattern Analysis and Machine Intelligence, IEEE Transactions on* **26** (8), 1007–1019.
- JEFFERY, G. B. 1922 The motion of ellipsoidal particles immersed in a viscous fluid. *Proceedings of the Royal Society of London. Series A, Containing Papers of a Mathematical and Physical Character* **102** (715), pp. 161–179.
- KAFTORI, D., HETSRONI, G. & BANERJEE, S. 1995a Particle behavior in the turbulent boundary layer. I. motion, deposition, and entrainment. *Physics of Fluids* **7** (5), 1095–1106.
- KAFTORI, D., HETSRONI, G. & BANERJEE, S. 1995b Particle behavior in the turbulent boundary layer. II. velocity and distribution profiles. *Physics of Fluids* **7** (5), 1107–1121.
- LUNDELL, F., SÖDERBERG, L. D. & ALFREDSSON, P. H. 2011 Fluid mechanics of papermaking. *Annual Review of Fluid Mechanics* **43** (1), 195–217.

- MARCHIOLI, C., FANTONI, M. & SOLDATI, A. 2010 Orientation, distribution, and deposition of elongated, inertial fibers in turbulent channel flow. *Physics of Fluids* **22** (3), 033301.
- MARCHIOLI, C. & SOLDATI, A. 2002 Mechanisms for particle transfer and segregation in a turbulent boundary layer. *Journal of Fluid Mechanics* **468**, 283–315.
- MORTENSEN, P., ANDERSSON, H., GILLISSEN, J. & BOERSMA, B. 2008 On the orientation of ellipsoidal particles in a turbulent shear flow. *International Journal of Multiphase Flow* **34** (7), 678 – 683.
- NARAYANAN, C., LAKEHAL, D., BOTTO, L. & SOLDATI, A. 2003 Mechanisms of particle deposition in a fully developed turbulent open channel flow. *Physics of Fluids* **15** (3), 763–775.
- NINTO, Y. & GARCIA, M. H. 1996 Experiments on particlewall region of an open channel flow: implications for sediment transport. *Journal of Fluid Mechanics* **326**, 285–319.
- TSUKAHARA, T., SEKI, Y., KAWAMURA, H. & TOCHIO, D. 2005 DNS of turbulent channel flow at very low reynolds numbers. In *Proc. of the Forth Int. Symp. on Turbulence and Shear Flow Phenomena*, pp. 935–940.
- WHITE, C., SOMANDEPALLI, V. & MUNGAL, M. 2004 The turbulence structure of drag-reduced boundary layer flow. *Experiments in Fluids* **36**, 62–69.
- ZACKSENHOUSE, M., ABRAMOVICH, G. & HETSRONI, G. 2001 Automatic spatial characterization of low-speed streaks from thermal images. *Experiments in Fluids* **31** (2), 229–239.
- ZHANG, H., AHMADI, G., FAN, F.-G. & MCLAUGHLIN, J. B. 2001 Ellipsoidal particles transport and deposition in turbulent channel flows. *International Journal of Multiphase Flow* **27** (6), 971 – 1009.
- ZHAO, L. H., ANDERSSON, H. I. & GILLISSEN, J. J. J. 2010 Turbulence modulation and drag reduction by spherical particles. *Physics of Fluids* **22** (8), 081702.

Paper 2

2

Measurement of width and streakiness of particle streaks in turbulent flows

By **Karl Håkansson**^{1,2}, **Mathias Kvick**^{1,2}, **Fredrik Lundell**^{1,2},
Lisa Prahl Wittberg^{1,2} and **L. Daniel Söderberg**^{1,3}

¹ Wallenberg Wood Science Center, KTH Mechanics, Royal Institute of Technology, SE – 100 44, Stockholm, Sweden

² Linné Flow Centre, KTH Mechanics, Royal Institute of Technology, SE – 100 44, Stockholm, Sweden

³ Innventia AB, BOX 5604, SE-114 86, Stockholm, Sweden

Submitted

Fibre streaks are observed in experiments with fibre suspensions in a turbulent half channel flow. The preferential-concentration method, most commonly used to quantify preferential particle concentration, is found to break down at low concentrations.

Two different new streak quantification methods are evaluated, one based on Voronoi analysis and the other based on artificial particles with an assigned fixed width. The width of the particle streaks, and a measure of the intensity of the streaks, *i.e.* streakiness, are sought. Both methods are based on the auto-correlation of a signal, generated by summing images in the direction of the streaks. Common for both methods is a severe concentration dependency, verified in experiments keeping the flow conditions constant while the (very dilute) concentration of fibres is altered.

The fixed width method is shown to be the most suitable method, being more robust and less computationally expensive. By assuming the concentration dependence to be related to random noise, an expression is derived, that is shown to make the streak width and the streakiness independent of the concentration even at as low concentrations as 0.05 particles per column in an image. The streakiness is obtained by applying an artificial particle width equal to 20% of the streak width. This width is in this study found to be large enough to smoothen the correlation without altering the streakiness nor the streak width. It is concluded that in order to make quantitative comparisons between different experiments or simulations, the evaluation has to be performed with care and be very well documented.

1. Introduction

When introducing particles into a turbulent wall bound-ed flow, it is well known that the particles tend to agglomerate into streamwise streaks close to the walls. This has been found both in experiments, *e.g.* (Rashidi *et al.* 1990; Fessler *et al.* 1994; Kulick *et al.* 1994; Kaftori *et al.* 1995*a,b*; Ninto & Garcia 1996), and in simulations, *e.g.* (Pedinotti *et al.* 1992; Rouson & Eaton 2001; Narayanan *et al.* 2003; Marchioli *et al.* 2010).

In many industry processes, *e.g.* paper making, particle suspensions are pumped and transported through different geometries at high speeds, resulting in turbulent wall bounded flows. In order to understand how the particles are influenced by the turbulent flow, it is important to obtain a quantitative measure of the strength of the tendency for the particles to agglomerate into streaks. This is also necessary if different experiments and simulations are to be compared.

Even though several methods exist to investigate clustering, these methods are not able to provide information whether particles form streaks or not.

Fessler *et al.* (1994) introduced the parameter D , quantifying 2-dimensional preferential concentration, defined by comparing the measured particle density to a random distribution;

$$D = \frac{\sigma - \sigma_p}{\lambda} \quad (1)$$

where σ is the standard deviation of the measured particle density, σ_p is the standard deviation of a random Poisson distribution and λ is the mean particle density. D becomes positive if clusters and voids are present, negative if the particle distribution is homogeneous and zero if the particles are randomly distributed. The parameter D is dependent of the box size, and by finding the box size that maximizes D , the typical cluster size can be found.

A more recent preferential concentration quantification method, based on Voronoi analysis, was proposed by Monchaux *et al.* (2010). In a Voronoi analysis, each particle is assigned a cell with an area inversely proportional to the local concentration. Comparing measured cell areas to a Poisson distribution provides the location and characterization of clusters.

The preferential concentration parameter D will be shown to be concentration dependent and thus failing to provide a consistent measure of the typical cluster size. The Voronoi analysis method displays a similar behavior. Therefore, in order to characterize the 1-dimensional streaks, more information is needed, emphasizing the need of a new method.

In this article, correlations in the spanwise direction, normal to the streaks, will be used to determine (i) a streak width and (ii) an objective quantification of the qualitative term "streakiness" (tendency to agglomerate in streaks). This correlation will be obtained in two ways, both of which make use of the position of individual particles in an image. The first is based on a Voronoi analysis; the

second is a straightforward correlation similar to a sum of image intensities. The second method is determined to be most suitable. As a result a scheme to determine the streak width and the streakiness independent of particle size, orientation, concentration, image size and streak width is obtained, including a consistent way of setting the one input parameter. The dependence of:

- particle size and orientation is treated by identifying the center of gravity of the particles in the images.
- concentration effects on the correlation is treated using the correlation from an image with randomly placed particles.
- image size is treated by considering the finite length of the input signal into the correlation.
- streak width is treated by normalizing the input parameter with the streak width (iterations are needed).

2. Methods

2.1. Flow apparatus

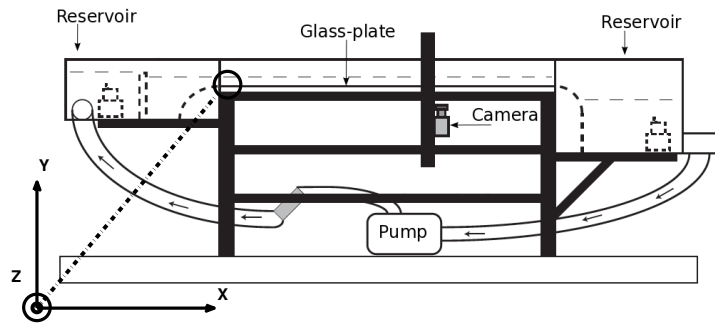


FIGURE 1. Schematic of the flow apparatus

Images of a fibre suspension in a turbulent half channel flow have been acquired. Fig. 1 depicts the flow apparatus where the suspension is pumped from a downstream to an upstream reservoir, allowing the suspension to flow down an inclined glass plate. A camera is mounted underneath the glass plate acquiring images of the fibres in the flow. A typical image is shown in Fig. 2, showing clearly that fibres form streaks. Pumps are placed in the upstream and downstream reservoirs in order to stir the suspension, and prevent fibres from sedimenting in the reservoirs. The coordinate system is defined so that the x -axis correspond to the streamwise direction, the y -axis is in the wall normal direction and the z -axis is in the spanwise direction. The origin is positioned on the leading edge of the glass plate with $z = 0$ on its centreline.

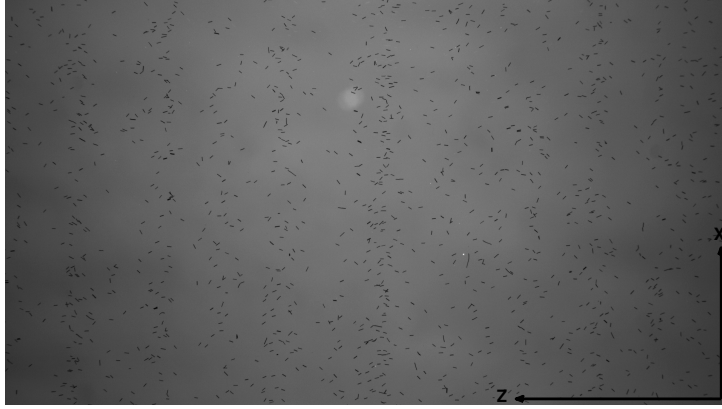


FIGURE 2. Example of an image from a turbulent fibre suspension flow with clear fibre streaks. The fibres are black, the differences in intensity are mostly due to the focusing of the light source, the flow is from bottom to top

Velocity profiles of the flow were measured with Laser Doppler Velocimetry (LDV) at the acquisition point, upstream of the acquisition point and also at two spanwise positions. The velocity profiles showed good agreement with DNS data for a full channel and the flow was confirmed to be turbulent and fully developed. More details regarding the setup and the LDV measurements can be found in Kvik *et al.* (2012), where the same setup was used.

Since the flow is driven by gravity alone, the wall shear stress, τ_w , can be calculated through the force balance at the wall;

$$\tau_w = \rho g h \sin \alpha. \quad (2)$$

Here ρ represents the density of the fluid, g is the gravitational acceleration, h is the height of the water layer on the glass plate and α is the inclination angle of the plate. The friction Reynolds number is defined as;

$$Re_\tau = \frac{h u_\tau}{\nu} = \frac{h \sqrt{g h \sin \alpha}}{\nu}, \quad (3)$$

where $u_\tau = \sqrt{\tau_w / \rho}$ and ν represent the friction velocity and the kinematic viscosity, respectively.

The suspension consists of water and cellulose acetate fibres with density 1300 kg/m^3 and concentrations $nl^3 = 0.0007 - 0.006$. For each case, 150 statistically independent images (1920×1080 pixels) are acquired, *i.e.* all fibres are transported out of the field of view of the camera before the next image is taken.

TABLE 1. Table of experiments with different concentration of fibres.

Case	Re_τ	r_p	c	Physical conc.	Artificial conc.
1	110	7	0.12	●	○
2	110	7	0.46	■	□
3	110	7	0.55	◀	◁
4	110	7	0.75	▶	▷
5	110	7	0.97	▼	▽

The positions of the fibres in the images are obtained by the use of a steerable filter, described in Carlsson *et al.* (2011). Using this filter, it is possible to detect both fibre positions and orientations in the flow-vorticity plane. The filter can even detect crossed fibres to a certain degree. Several layers of fibres or fibres covering most of the image can not be identified by the filter. This is one of the reasons to why the experiment has to be performed at low concentrations of fibres in the suspension. With index of refraction matching methods (where a only a fraction of the actual particles are visible), higher particle concentrations can be reached. However, the concentration of visible particles would still be limited, since the detection is dependent of the resolution of the camera and the size of the particles.

To evaluate the different analysis methods, the experiments are performed using constant Re_τ and aspect ratio, but different fibre concentrations. This is referred to as physical concentration in this study. An artificial concentration variation is also used, by detecting and identifying all fibres in the images, and randomly excluding fibres during post processing. Note that aspects such as streakiness and streak width should be constant during the artificial concentration variation, since the fibres are removed randomly.

Firstly, five experiments at $Re_\tau = 110$, with fibres of aspect ratio $r_p = 7$ and varying fibre concentration will be considered. The particle (fibre) concentration, c , are measured in particles (fibres) per column of pixels in the image. The specifications for the five cases are displayed in table 1. Case 3, where clear streaks are observed, will be used as an example to illustrate differences in the two new analysis methods. Thereafter quantitative results from five other cases ($Re_\tau = 51 - 178$) will be shown in order to highlight differences in streakiness. Finally the experiments with different concentration will be considered.

2.2. Preferential concentration parameter, D

The preferential concentration parameter, D , defined in equation 1, is in this 1-dimensional case calculated using columns in the direction of the streaks instead of boxes. The width of the columns are varied and the resulting values of D are displayed in Fig. 3. Fig. 3 shows cases 1-5 where only the concentration has been varied, $0.12 < c < 0.97$ particles per column. It can be concluded that

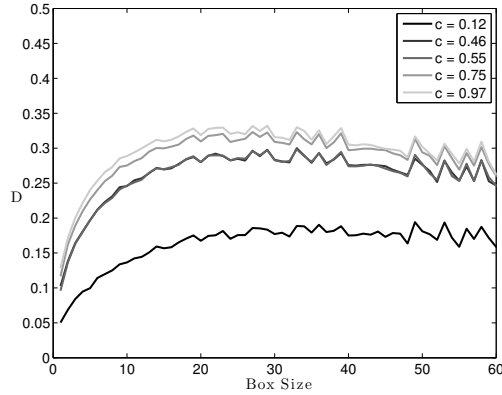


FIGURE 3. The preferential concentration parameter, D , versus box size in pixels

D is concentration dependent, and the jagged appearance of the curves makes it difficult to determine what a typical streak size would be. In this kind of flow the streaks are expected to appear at random streamwise positions, but having a similar size (width), as the case for low and high velocity streaks in e.g. Lagraa *et al.* (2004). Due to the concentration dependence and the many peaks of the D -curves in Fig. 3, further development of the method is needed, or a new approach needs to be developed. The latter is pursued in this study.

2.3. Correlation based analysis

The analysis methods presented in this paper are based on auto-correlating a discrete signal obtained from an image, the correlation curves are used to quantify the streaks. The signal is denoted, I , and the auto-correlation of the signal, R_{II} , is defined as:

$$\hat{R}_{II}(\Delta z) = \int I(z + \Delta z)I(z)dz, \quad R_{II} = \frac{\hat{R}_{II}}{\max \hat{R}_{II}}. \quad (4)$$

The signal used in the correlations are obtained in different manners by the two different methods. However, the basic idea is the same: summing intensities in the direction along the streaks. A straightforward way of obtaining the signal is to sum the intensities of the raw images in the streaky direction. This is similar to standard investigations of high and low velocity streaks in turbulent or transitional boundary layers, see e.g. Lagraa *et al.* (2004) or Fransson & Alfredsson (2003). In this way, information regarding the sizes and strengths of the structures can be extracted fairly easy.

However, using raw images as input into the analysis, several problems arises. One is the effect of differences in light intensities in the image. Another

important aspect is the influence of the particle orientation in case of non-spherical particles. The signal will have a very different appearance depending on if the particles are oriented in the summing direction or perpendicular to it. To be able to assess these problems, it is necessary to use only the particle positions, and thereby reducing the number of non-controllable parameters.

The position and orientation of each particle are found in a first post processing step as mentioned earlier. With the positions known, the control over the input into the analysis is very high and comparable to the data from Lagrangian simulations.

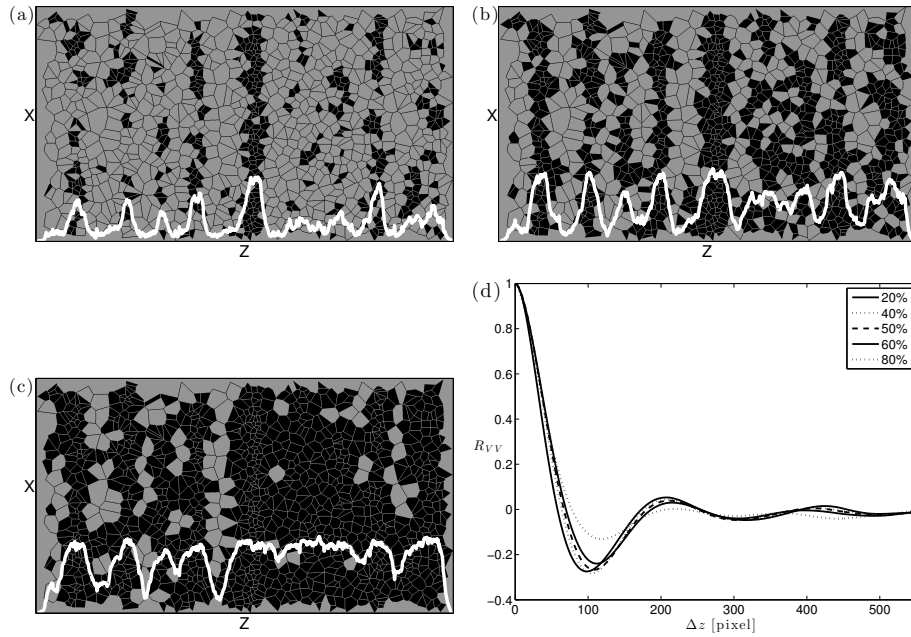


FIGURE 4. Voronoi map of the image in Fig. 2 with threshold (a) 20%, (b) 50% and (c) 80%, considered clustered with a high local density and here colored black, the resulting signal for each image is colored white. (d) R_{VV} for the complete set. The percentages in the legend corresponds to the part of the images considered to belong to streaky regions, and therefore contributing to the signal

2.4. Correlations based on Voronoi analysis

In order to obtain an analysis method independent of particle width and orientation, a Voronoi tessellation is applied to the particle positions. In a Voronoi

diagram, the image is divided into an unstructured grid with one particle in each cell. The size and shape of each cell is determined by the surrounding particles. Particles located in regions with high local concentration has small cell areas and particles in regions where the concentration is lower has larger cell areas.

Thresholding the distribution of cell areas makes it possible to control the cells that are to be regarded as clustered and located in streaks, corresponding to small areas. Assigning a value, *e.g.* 1, to the small areas and summing the image in the streamwise direction results in a signal that can be auto-correlated.

Fig. 4a–4c shows different thresholds for a Voronoi diagram based on Fig. 2, together with the resulting signals. In Figs. 4a–4c, 20%, 50% and 80% of the total image area is regarded as clustered cells, respectively. The clustered cells are colored black (value 1), and a summation of the images in the streaky direction (vertical) results in the signals displayed in white.

The signals are auto-correlated and the mean of the auto-correlations for all 150 images in the measurement set is displayed in Fig. 4d. The Voronoi based correlations, denoted R_{VV} , vary for different thresholds but display a lowest minimum for a threshold close to 50%. 50% is used as the threshold value in the rest of this paper. There are other options to threshold. For example, use the deviation of a random distribution of cell areas as the threshold, see *e.g.* Monchaux *et al.* (2010). Due to the low concentrations used in the present study, the thresholds were inconsistent.

2.5. Correlations based on a fixed width

The second method uses the positions of the physical particles to construct images with artificial particles.

In order to smoothen the signal, the width, w , of the artificial particles is fixed to a value larger than one pixel. In Fig. 5a - 5c, three choices of particle widths are shown, based on the image in Fig 2. The sums of these artificial images are shown in black and, as is evident, the particle width influences the signal. Furthermore, as can be seen in Fig. 5d showing the correlation R_{ff} for the different particle widths, the choice of particle width plays an important role for the resulting correlation and must not be greater than the streak width. A particle width larger than the streak width results in that the small peaks are filtered out. In Fig. 5d it is noted that the correlations first zero crossing does not change significantly until the particle fixed width exceeds 41 pixels.

2.6. Determination of streak width, $2\Delta z(R_{II} = 0)$, and streakiness, $\Xi(R_{II})$, from correlations

The streak width is in this study determined as the displacement at which the minimum correlation occurs. However, this point is never well defined. Therefore the first zero-crossing, that can be interpolated, is taken as the streak

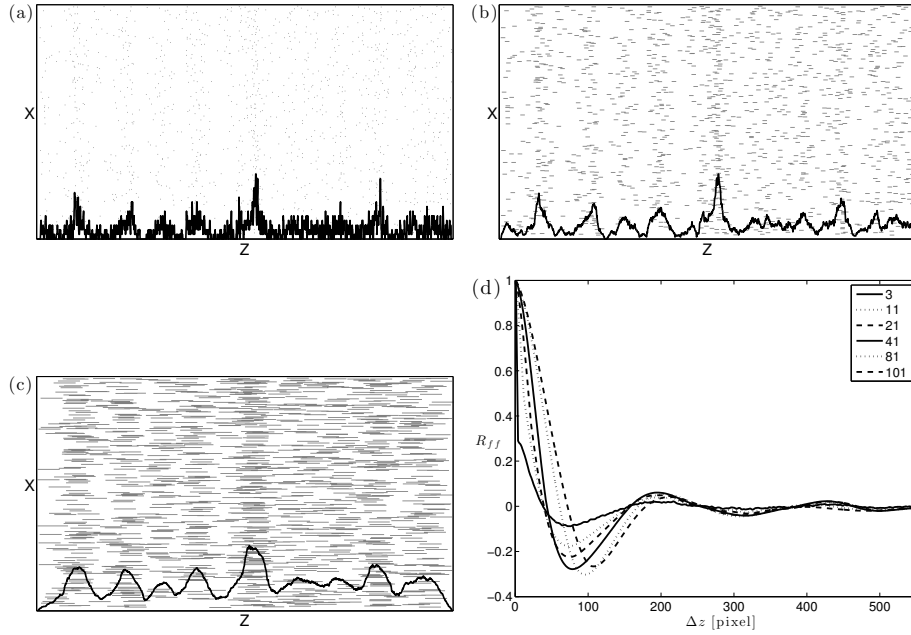


FIGURE 5. Determination of horizontal correlation using particle position from the image in Fig. 2. (a) Image with fixed particle width $w = 3$ pixel and vertical sum of this figure, (b) image with fixed particle width $w = 21$ pixels and vertical sum of this figure, (c) image with fixed particle width $w = 101$ pixels and vertical sum of this figure, (d) correlations for $w = 3, \dots, 101$ pixels

half width, $\Delta z(R_{II} = 0)$, where $R_{II} = 0$ implies the first position at which the correlation is zero. The same approach was used for velocity streaks by Fransson & Alfredsson (2003) and shown to be consistent.

The minimum value of the correlation is a measure of how coherent the particle structures are, *i.e.* a measure of the strength of the streaks. The streakiness is from here on defined as; $\Xi(R_{II}) = |\min(R_{II})|$. A lower negative minimum value of the correlation implies higher or stronger streakiness. In other words that the particle structures in the flow are more coherent.

3. Results and Discussion

3.1. Fixed width vs. Voronoi based correlation

In Fig. 6, the correlation of the Voronoi based analysis with a threshold of 50% is depicted together with the correlation using the fixed width method with a

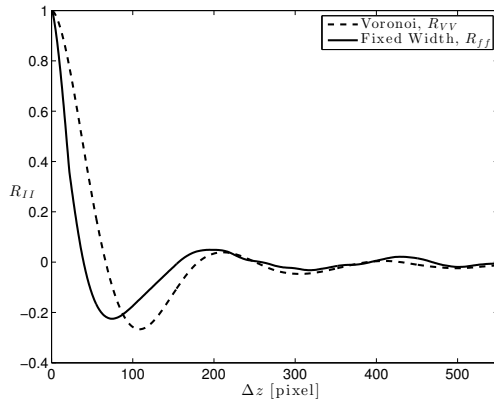


FIGURE 6. Comparison of the Voronoi based correlation, R_{VV} , and the fixed width based correlation, R_{ff} , where the fixed width has been set to 21 pixels and the threshold in the Voronoi analysis to 50%

particle width of 21 pixels. It can be seen that the Voronoi based method gives a lower minimum and is shifted to the right. The reason for the shift of the correlation curve will be shown to be due to the concentration dependency. An evaluation of the concentration dependency of both methods, and a solution in order to obtain the streakiness and streak width independent of concentration is described below.

3.2. Effect of number of particles

3.2a. *Streakiness*, $\Xi(R_{II})$. The number of particles in each image (concentration) affects the analysis independently of the method used. Since experimental images will have a fairly low concentration (even if index-of-refraction has been used and the actual concentration is quite high), the method needs to be able to handle low concentrations. In order to investigate how the concentration affects the outcome of the different analysis methods, experiments with different concentrations of particles in the suspension were performed, while the flow conditions were kept constant.

The other way of changing the concentration is random removal of particles from the pictures during post processing. In Fig. 7a and 7b, the streakiness, $\Xi(R_{ff})$, versus the number of particles per column, c , are shown, using the fixed width method. Fig. 7a depicts results from a physical concentration variation and 7b the artificial concentration variations for five different flow cases. The symbols (\otimes , $*$, \oplus , \blacklozenge , \blacktriangle) represent the original measurements in 7b and the symbols (\circ , \times , $+$, \diamond , \triangle) represent the artificial variations of concentration, where the

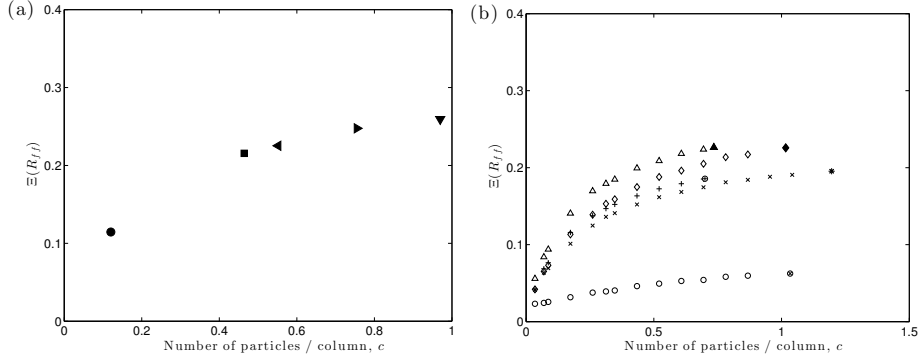


FIGURE 7. Streakiness as a function of concentration using (a) experimental and (b) artificial variation. In (b) several cases corresponding to different Reynolds numbers and concentrations are shown, ($\otimes, *, \oplus, \blacklozenge, \blacktriangle$) is the original concentration and ($\circ, \times, +, \diamond, \triangle$) are the artificial variations. Each symbol pair belongs to one experimental case. The fixed width method was used in both (a) and (b)

Reynolds' numbers used are $Re_\tau = 51, 178, 167, 71$ and 88 , respectively. The different experiments have different concentrations and different streakiness.

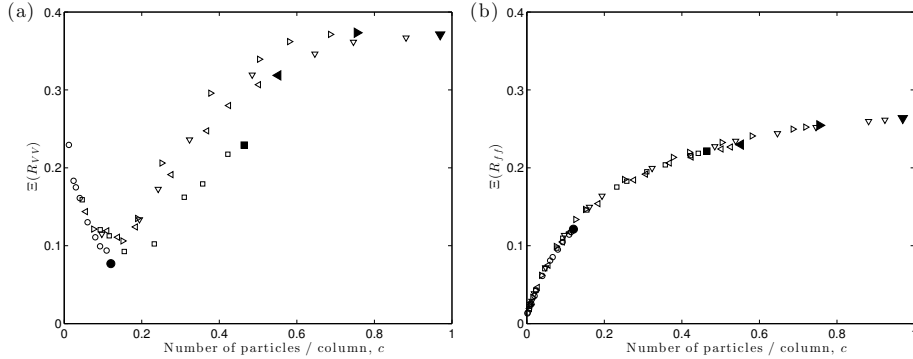


FIGURE 8. Scaling of streakiness for different number of particles, both physical ($\bullet, \blacksquare, \blacktriangleleft, \blacktriangleright, \blacktriangledown$) and artificial ($\circ, \square, \triangleleft, \triangleright, \triangledown$) concentration variations, (a) using Voronoi based correlation and (b) using fixed width correlation

In Fig. 8a the Voronoi based method is used and both physical, ($\bullet, \blacksquare, \blacktriangleleft, \blacktriangleright, \blacktriangledown$), and artificial, ($\circ, \square, \triangleleft, \triangleright, \triangledown$), concentration variations are performed. The

similarity between the two different concentration variations using the Voronoi method is poor. In Fig. 8b it is shown that by excluding particles in the post processing it is possible to recreate the behavior observed in the experiments using the fixed width method. Note that a naive interpretation of the data in Fig. 7a is that the streakiness varies with concentration, whereas Fig. 8b shows that this variation is an artifact of the evaluation. In section 3.3, corrections for this artifacts are derived and demonstrated to give a consistent quantification of the streakiness.

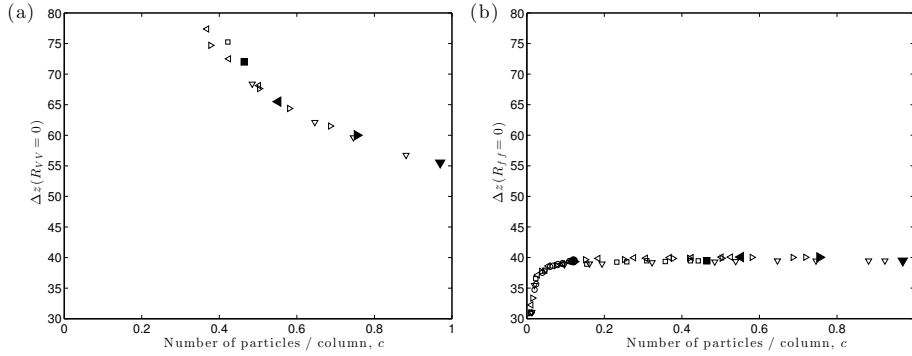


FIGURE 9. Streak width for different number of particles, both physical ($\bullet, \blacksquare, \blacktriangleleft, \blacktriangleright, \blacktriangledown$) and artificial ($\circ, \square, \triangleleft, \triangleright, \triangledown$) concentration variations, (a) using Voronoi based correlation and (b) using fixed width correlation

3.2b. *Streak width, $2\Delta z(R_{II} = 0)$.* Fig. 9 shows both physical ($\bullet, \blacksquare, \blacktriangleleft, \blacktriangleright, \blacktriangledown$) and artificial ($\circ, \square, \triangleleft, \triangleright, \triangledown$) concentration variations of the streak half width in pixels. The Voronoi based method and the fixed width method are displayed in Fig. 9a and 9b, respectively. The fixed width method has a stable streak width for concentrations greater than ~ 0.1 particles per column. The Voronoi method on the other hand display a significant variation in streak width, explaining the shift of the Voronoi correlation curve as shown in 6. The behavior of the Voronoi analysis is logic; less particles leads to a larger average cell size, resulting in a larger streak width.

3.3. Obtaining a consistent measure

When comparing the two methods, three major advantages can be found for the fixed width method: (i) the streak width is independent of the concentration, (ii) the collapse of the physical and artificial concentration variation is better and (iii) it is computationally cheaper as compared to the Voronoi based method. Due to the above mentioned advantages, the fixed width method is

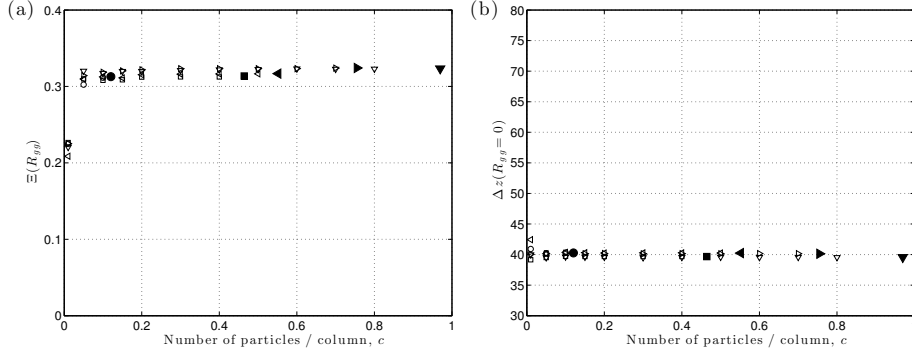


FIGURE 10. (a) Streakiness and (b) streak widths for different number of particles, both physical (\bullet , \blacksquare , \blacktriangleleft , \blacktriangleright , \blacktriangledown) and artificial (\circ , \square , \triangleleft , \triangleright , \triangledown) concentration variations, from the true correlation R_{gg} (equation 7)

the approach that will be considered and improved so that consistent measures are obtained. The aspects that needs to be taken into account are concentration, and the artificial particle width w . The latter needs to be considered in relation to the actual streak width why an iteration will be needed in order to find w .

In order to determine the relative streakiness, the particles are first located and given a width, the image is summed in the streak direction to obtain the signal. Thereafter, the auto-correlation is computed using the resulting signal. If the concentration between the measurements is not constant, this needs to be taken into account. Note that this implies that the procedure below has to be applied before concentration effects of streakiness are deduced.

3.3a. *Concentration.* The concentration dependence is reduced by first assuming that the signal $I = f(z, c)$ consists of a true signal $g(z, c)$ and a perturbation $g'(z, c)$, both dependent on the concentration $c \in [0, \infty]$, as;

$$f(z, c) = g(z, c) + g'(z, c). \quad (5)$$

The auto-correlation $\hat{R}_{ff}(\Delta z, c)$ can be split into three parts;

$$\begin{aligned} \hat{R}_{ff}(\Delta z, c) &= \\ &= \hat{R}_{gg}(\Delta z, c) + \hat{R}_{gg'}(\Delta z, c) + \hat{R}_{g'g'}(\Delta z, c), \end{aligned} \quad (6)$$

where the correlations are not yet normalized. If the perturbation g' and the true signal g are independent of each other the correlation $\hat{R}_{gg'}$ will be zero, and this is assumed. The last term, $\hat{R}_{g'g'}$, will be taken as the auto-correlation of a random image with concentration c and artificial particle width w . This

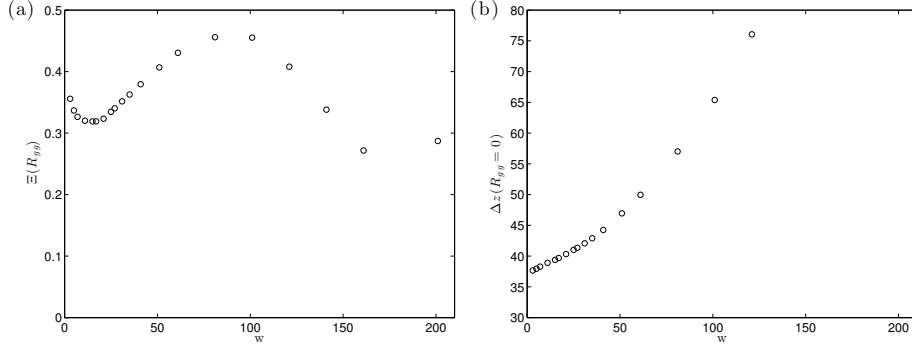


FIGURE 11. Streakiness (a) and streak widths (b) for different artificial particle width, w . The concentration 0.1 particles per column is used

correlation can be computed by placing particles at random positions, thus producing an artificial signal where the parameters c and w have been chosen to match the ones used for the experimental images.

When $\hat{R}_{gg'}$ is set to zero, and c and w are known, a perturbation-corrected correlation is obtained from equation 6 as:

$$R_{gg} = \frac{\hat{R}_{ff} - \hat{R}_{g'g'}}{\max(\hat{R}_{ff} - \hat{R}_{g'g'})}, \quad (7)$$

where the last step is to normalize the correlation.

The streakiness and the streak width extracted from the true correlation R_{gg} , in turn calculated from equation 7 are shown in Figs. 10a and 10b, respectively. As before, (\bullet , \blacksquare , \blacktriangleleft , \blacktriangleright , \blacktriangledown) represents physically varied concentration and (\circ , \square , \triangleleft , \triangleright , \triangledown) represents artificially varied concentrations. In Fig. 10a, the apparent concentration dependency of the streakiness in cases 1-5 from Fig. 7a is cancelled for concentrations greater than ~ 0.05 particles per column. Regarding the streak width, the concentration dependency is observed to be even better improved. For concentrations lower than 0.05 the assumption that g and g' are independent may not be true.

3.3b. *Artificial particle size w .* The solely free parameter is the artificial particle width. Fig. 11 depicts how (a) the streakiness and (b) the streak width vary with the artificial particle width for case 1. It is clear that both of these sought quantities depend on w . The streak width increases with increasing w , while the streakiness on the other hand, first assumes a minimum and then a maximum as w increases. It should be noted that the maximum occurs at a particle width much larger compared to the streak width and is therefore disregarded.

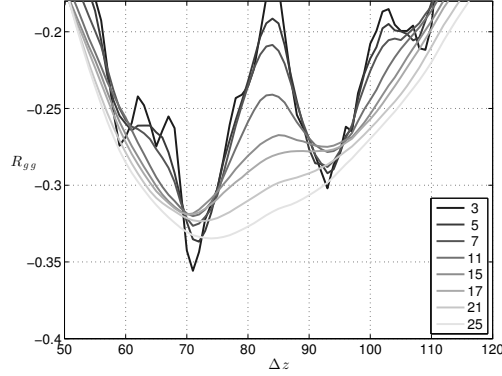


FIGURE 12. Close up off the correlation minima for different w for the same case as in Fig. 11

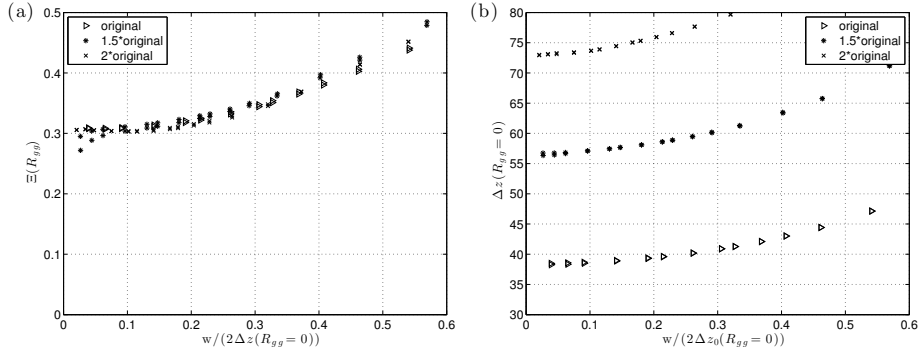


FIGURE 13. Streakiness (a) and streak widths (b) for different streak widths, a collapse of the curves is seen when plotted against $w/2\Delta z(R_{gg} = 0)$ in (a). Original streak width, (\triangleright), all particle positions multiplied by 1.5, ($*$) and 2, (\times). The image size is kept constant and two concentrations are used (0.1 and 0.2 particles per column)

In Fig. 12 a close up of the correlation minima for $w = 3, 5, 7, 11, 15, 17, 21, 25$ pixels are displayed, corresponding to the eight lowest w -values in Fig. 11a and 11b. As w increases the correlation is seen to become smoother, explaining the minimum in Fig. 11a. As low value as possible for w is wanted, but the correlation must be smooth enough to have a well defined minimum.

3.3c. *Streakiness dependence on streak width.* Since the positions of all particles are known it is easy to test the dependency of streakiness on streak width.

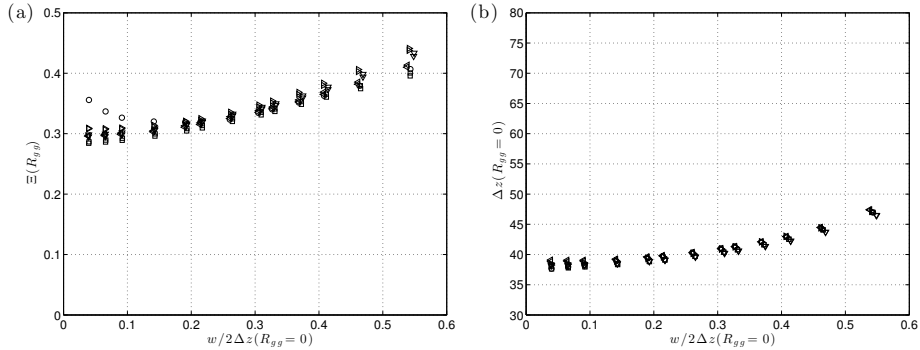


FIGURE 14. Streakiness (a) and streak widths (b) for different artificial particle width, w . Cases 1-5 with two concentrations, 0.1 and 0.2 particles per column, each are displayed (\circ , \square , \triangleleft , \triangle , ∇)

When the streak width is artificially changed by multiplying all particle positions with a constant, the effect on the streakiness can be observed. Preferably the streakiness would be constant. Fig. 13 displays three different cases, first the original case (\triangleright), and also two cases where the positions of all particles have been multiplied by the factors 1.5 ($*$) and 2 (\times). The image size is kept constant. When w is normalized with the streak width, $2\Delta z(R_{gg} = 0)$, the curves collapse.

The image finite size finally also needs to be accounted for, due to the loss in information in the auto-correlation. The correlations in Fig. 13 are therefore normalized with $(1 - \Delta z/\text{image size})$, and so are all results from here on. This step makes the method independent of image size, Isermann & Münchhof (2011).

The information from this section shows that it is possible to compare the streakiness qualitatively between two different experiments if the same value of $w/2\Delta z(R_{gg} = 0)$ is used, and the image size is taken into account through the normalization above.

3.3d. *Streakiness at $w/2\Delta z(R_{gg} = 0) = 0.2$, $\Xi(R_{gg})_{0.2}$.* The final streakiness values, $\Xi(R_{gg})$, and streak widths, $\Delta z(R_{gg} = 0)$ are plotted against the artificial particle width normalized by the streak width in Fig. 14. The concentrations shown are 0.1 and 0.2 particles per column for the five cases, (\circ , \square , \triangleleft , \triangle , ∇), except for the lowest concentration case that has a physical concentration of only 0.12 particles per column. The spread of $\Xi(R_{gg})$, due to jagged correlations at small $w/2\Delta z(R_{gg} = 0)$, for the lowest concentration (\circ), is the reason for the streakiness to be taken as the value at $w/2\Delta z(R_{gg} = 0) = 0.2$. A subscript is introduced to the streakiness notation, $\Xi(R_{gg})_{0.2}$, in order to indicate

which relative particle width that is used. At $\Xi(R_{gg})_{0.2}$ both streakiness and streak width starts to increase, but the deviations up to this point are small.

4. Conclusions

A method that provides consistent measures of streakiness and streak width in particle images from different flow situations has been developed and verified. The final method is independent of particle concentration, image size and streak width as well as the parameters of the method itself.

First, two particle streak analysis methods have been compared and evaluated. The two methods were based on particle positions, summation of images and a following correlation. The streak width and the streakiness were sought. The streak half width, Δz , was taken as the first zero-crossing of the correlation and the streakiness, $\Xi(R_{II}) = |\min(R_{II})|$. The first method was based on Voronoi analysis and the second on artificial particles with an assigned fixed width. Both methods were shown to possess a severe concentration dependence.

However, the streak width was shown to be constant at concentrations greater than ~ 0.1 particles per column for the fixed width method. The fixed width method was improved and an expression was derived to account for the concentration dependence of the streakiness. The derivation was based on a random image significantly contribute to the total correlation at low concentrations. After this correction, the streakiness was shown to be independent of concentrations lower than ~ 0.05 particles per column. Furthermore, scaling the artificial particle width with the streak width made the streakiness independent of streak width. Therefore, and because of the need to smoothen the correlation, it is proposed to set the artificial particle width to 20% of the streak width, denoted $\Xi(R_{gg})_{0.2}$.

5. Acknowledgements

Mr Joseph Fjellgren is acknowledged for the schematic drawing of the setup. This work was funded by the Knut and Alice Wallenberg Foundation, through the Wallenberg Wood Science Center. Dr. Lundell and Dr. Prah Wittberg has also been funded by the Swedish Research Council.

References

- CARLSSON, A., HÅKANSSON, K., KVICK, M., LUNDELL, F. & SÖDERBERG, L. D. 2011 Evaluation of steerable filter for detection of fibers in flowing suspensions. *Experiments in Fluids* **51**, 987–996.
- FESSLER, J. R., KULICK, J. D. & EATON, J. K. 1994 Preferential concentration of heavy particles in a turbulent channel flow. *Physics of Fluids* **6** (11), 3742–3749.
- FRANSSON, J. H. M. & ALFREDSSON, P. H. 2003 On the disturbance growth in an asymptotic suction boundary layer. *Journal of Fluid Mechanics* **482**, 51–90.
- ISERMANN, R. & MÜNCHHOF, M. 2011 Correlation analysis with discrete time models. In *Identification of Dynamic Systems*, pp. 179–200. Springer Berlin Heidelberg.
- KAFTORI, D., HETSRONI, G. & BANERJEE, S. 1995*a* Particle behavior in the turbulent boundary layer. I. motion, deposition, and entrainment. *Physics of Fluids* **7** (5), 1095–1106.
- KAFTORI, D., HETSRONI, G. & BANERJEE, S. 1995*b* Particle behavior in the turbulent boundary layer. II. velocity and distribution profiles. *Physics of Fluids* **7** (5), 1107–1121.
- KULICK, J. D., FESSLER, J. R. & EATON, J. K. 1994 Particle response and turbulence modification in fully developed channel flow. *Journal of Fluid Mechanics* **277**, 109–134.
- KVICK, M., HÅKANSSON, K., LUNDELL, F., PRAHL-WITTBERG, L. & SÖDERBERG, L. D. 2012 Fibre orientation and fibre streaks in turbulent half channel flow. To be submitted.
- LAGRAA, B., LABRAGA, L. & MAZOUZ, A. 2004 Characterization of low-speed streaks in the near-wall region of a turbulent boundary layer. *European Journal of Mechanics - B/Fluids* **23** (4), 587–599.
- MARCHIOLI, C., FANTONI, M. & SOLDATI, A. 2010 Orientation, distribution, and deposition of elongated, inertial fibers in turbulent channel flow. *Physics of Fluids* **22** (3), 033301.
- MONCHAUX, R., BOURGOIN, M. & CARTELLIER, A. 2010 Preferential concentration of heavy particles: A Voronoï analysis. *Physics of Fluids* **22** (10), 103304.
- NARAYANAN, C., LAKEHAL, D., BOTTO, L. & SOLDATI, A. 2003 Mechanisms of particle deposition in a fully developed turbulent open channel flow. *Physics of Fluids* **15** (3), 763–775.

- NINTO, Y. & GARCIA, M. H. 1996 Experiments on particlewall region of an open channel flow: implications for sediment transport. *Journal of Fluid Mechanics* **326**, 285–319.
- PEDINOTTI, S., MARIOTTI, G. & BANERJEE, S. 1992 Direct numerical simulation of particle behaviour in the wall region of turbulent flows in horizontal channels. *International Journal of Multiphase Flow* **18** (6), 927–941.
- RASHIDI, M., HETSRONI, G. & BANERJEE, S. 1990 Particle-turbulence interaction in a boundary layer. *International Journal of Multiphase Flow* **16** (6), 935–949.
- ROUSON, D. W. I. & EATON, J. K. 2001 On the preferential concentration of solid particles in turbulent channel flow. *J. Fluid Mech.* **428**, 149–169.

Paper 3

3

Effects of nano-fibrillated cellulose on curvature- and rotation-induced instabilities in channel flow

By **Mathias Kvik**^{1,2}, **Fredrik Lundell**^{1,2}, **Lisa Prah**
Wittberg^{1,2} & **L. Daniel Söderberg**^{1,3}

¹ Wallenberg Wood Science Center, KTH Mechanics, Royal Institute of Technology, SE – 100 44, Stockholm, Sweden

² Linné Flow Centre, KTH Mechanics, Royal Institute of Technology, SE – 100 44, Stockholm, Sweden

³ Innventia AB, BOX 5604, SE-114 86, Stockholm, Sweden

May 14, 2012

Flow of a suspension of water and nano-fibrillated cellulose (NFC) in a curved and rotating channel is studied experimentally. The aim is to investigate how the NFC effects the stability of the flow. This flow is subject to a centrifugal instability creating counter-rotating vortices in the flow direction. These rolls can be both stabilised and de-stabilised by system rotation, depending on direction and rotation rate. Flow visualisation images with pure water and an NFC/water suspension are categorised and the resulting stability maps are compared. Stability analysis is performed and the effect of fibrils are taken into account assuming straight fibrils and constant orientation distributions, i.e. without the flow-orientation coupling. The results show that NFC stabilises the primary instability of the flow somewhat less than indicated from the viscosity increase measured by a rotary viscometer but more than predicted from the stability analysis. Several unknown parameters (the most prominent being fibril aspect ratio and the interaction parameter in the rotary diffusion) appear in the analysis.

1. Introduction

The aim of this work is to gain knowledge of curvature and rotation-induced instabilities of nano-fibrillated cellulose (NFC) suspensions. Nano-fibrillated cellulose, is a novel material made from wood. NFC is made by disintegrating paper pulp, consisting of fibres with an approximate length of 2 mm and a diameter of 100 μm . After disintegration, the nano fibrils have a length of order 2 μm and a diameter of 100 nm. Now, when this material starts to be integrated into established or new industrial processes, it becomes necessary to

understand how this addition will effect the flow. Here, a flow case and setup previously studied (with pure water) by Matsson & Alfredsson (1990) will be investigated.

A curved channel with a large aspect ratio on a rotating table is used. The curvature of the channel gives rise to a difference in centrifugal force depending on the velocity of the fluid, resulting in a Dean instability. This instability takes the form of counter rotating flow rolls in the streamwise direction (the primary instability). If the flow speed is further increased, wavy motions are observed on the rolls (secondary instability) and eventually, breakdown to turbulence will occur.

The rotation of the channel will induce a Coriolis force, which magnitude depends on the fluid velocity as well as the angular velocity. The Coriolis force either stabilises or destabilises the curvature-induced instability. Matsson & Alfredsson (1990) investigated the balancing effect of the Coriolis and centrifugal force and compared with results from linear stability theory. It was found that at certain rotational velocities the critical Reynolds number was substantially increased. Here, this rich stability problem will be used as a basis for NFC-suspension stability studies.

Research has previously been performed concerning the stability of fibril suspensions as well as polymer suspensions. Experimental results indicate that elongated particles stabilises certain instabilities, while at the same time destabilises others. Vaseleski & Metzner (1974) measured pressure drops in pipes of different diameters in order to investigate drag reduction of suspensions with nylon fibres, varying volume fractions and aspect ratios. They found that the transition to turbulence was delayed, i.e. the flow was stabilised. Pilipenko *et al.* (1981) on the other hand, found that the addition of plant fibres in a Taylor apparatus decreased the critical Taylor number and thereby destabilising the flow.

In contrast to the experimental results, conclusions from theoretical investigations are more coherent and show that fibres have a stabilising effect. Gupta *et al.* (2002) applied linear stability theory on a Taylor-Couette flow for a semi-dilute suspension containing non-Brownian fibres and found that, regardless of choice of closure approximation for the orientation tensor (these aspects will be returned to in more detail later), the critical Reynolds number was increased compared to a the case without fibres. The reason for the stabilisation was in this work suggested to be mainly due to fibre-fibre interactions.

Nsom (1996) investigated the effect of fibrils and gap-width on the stability of the flow in a curved channel. The critical wavelength was found to be unaffected by the presence of fibres, while in both the dilute and semi-dilute regimes, transition was delayed.

Azaiez (2000) studied the effects of fibres and polymers, separately, on a mixing layer, by means of linear stability. The stabilising effects of fibres

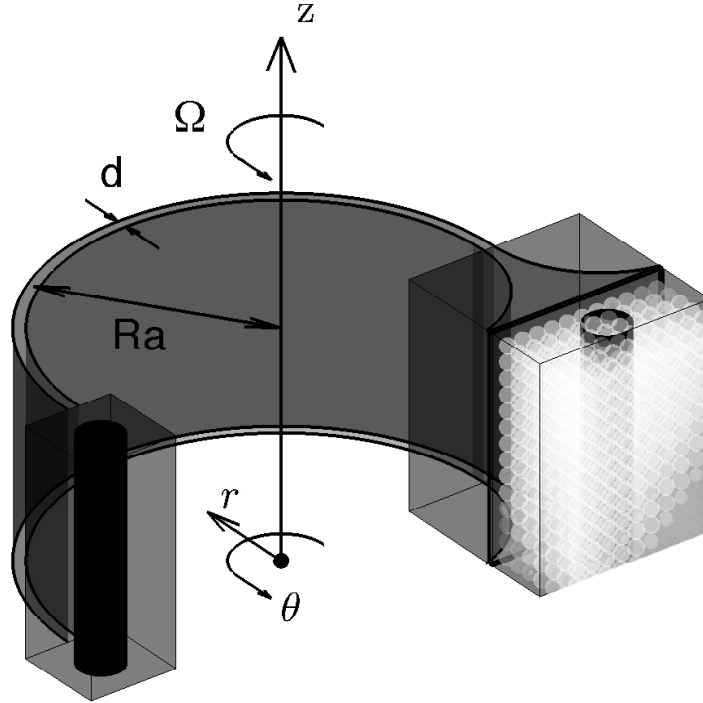


FIGURE 1. Schematic drawing of experimental apparatus. The inlet is located to the right in the figure, where packed glass spheres and a contraction are used to create a laminar inflow.

were determined to be a consequence of the orientational diffusivity due to hydrodynamic interactions. Zhenjiang *et al.* (2004) reported similar findings from a linear stability analysis of a fibre suspension flow in a rectangular channel and found that the addition of fibres not only stabilised the flow, but also increased the critical wavenumber.

In section 2 the experimental setup and the preparation of the suspension is explained. Section 3 describes the governing equations and the effect of fibrils on the linear stability equations. In section 4 the results are presented followed by a discussion and conclusions in sections 5 and 6.

2. Experimental methods

2.1. Experimental setup

The experimental apparatus was previously used by Matsson & Alfredsson (1990), comparing results from experiments with linear stability theory. The

curved channel covers 180° and has a radius of curvature of $Ra = 400$ mm. The channel has a width of 9.25 mm and a height of 280 mm.

The experimental setup is mounted on a table that can be rotated with angular velocities up to a maximum of 10 rpm in both directions. The flow rate is set by adjusting a valve before the inlet, and the outlet pressure is set with a valve located after the outlet. The flow rate is measured with a rotameter. A stagnation chamber is located prior to the channel, where packed glass beads are used in order to homogenise the flow and increase the pressure drop in the channel. Downstream of the stagnation chamber, two turbulence reducing screens are located. The screens, in addition with the contraction, are used in order to eliminate the disturbances at the inlet of the channel.

At a position 65 channel widths, d , downstream of the inlet, a CCD camera is mounted, capturing images of the flow. Two 500W halogen lights are used for illumination of the region of interest. In order to visualise the flow, a small amount of Iridin (plate-like particles that visualise flow structures), ~ 1.5 g, is added to the fluid with a total volume of 40 litres, having no impact on the properties of the fluid.

The flow is governed by the Reynolds number (Re) and the rotation number (Ro), defined as;

$$\text{Re} = \frac{U_b d}{\nu} \quad (1)$$

$$\text{Ro} = \frac{\Omega d}{U_b}, \quad (2)$$

where U_b is the bulk velocity acquired from flow rate measurements, d is the width of the channel, ν is the kinematic viscosity of the suspending fluid and Ω is the angular velocity. Experiments with pure water and NFC-suspension described below were carried out and will be compared with each other. During the experiments with the NFC-suspension, a limited accumulation of NFC occurred at some positions in the flow loop, resulting in a reduced concentration in the channel. This effect could not be quantified but is expected to be limited since the results are consistent comparing the first and final results of an experimental sequence.

2.2. The NFC suspension

The NFC has been prepared by an enzymatic pretreatment followed by a high pressure homogenisation at a concentration of 1% by weight, according to the procedure described by Pääkkö *et al.* (2007). The high pressure homogenisation was done at Innventia AB¹. The final concentration after the homogenisation was $c = 2\%$ by weight, at this concentration the NFC material is a gel. To further dilute the NFC-suspension to a much lower concentration as used in

¹Innventia AB, Box 5604, SE 114 86 Stockholm, Sweden

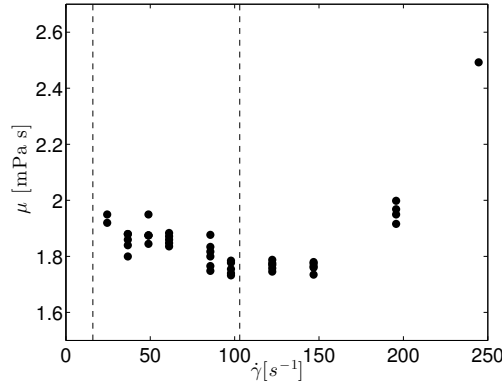


FIGURE 2. Shear viscosity data for the NFC suspension. The dashed lines indicate the minimum, $\dot{\gamma} = 16s^{-1}$, and maximum, $\dot{\gamma} = 103s^{-1}$, shear rates obtained at the wall in the experiments.

the experiments, $c = 400$ ppm by weight (corresponding to $nl^3 = 0.12$, where n is the number density per unit volume), a step wise process is adopted. In the process the concentration is halved and treated with a ultrasonic homogeniser in order to break up flocs, until the final concentration has been reached. Since the NFC used in this study had passed through the high pressure homogeniser only once, partial fibres were present in the final solution, that could not be broken with ultrasound.

The viscosity of the NFC suspension was measured using a rotational viscometer. In this study, no further effort was carried out in order to characterise the suspension. However, there are several ongoing efforts in this direction, *e.g.* Iotti *et al.* (2011), Puisto *et al.* (2012). The dynamic viscosity versus the shear rate is shown in figure 2, where several measurements was performed at the same shear rate, the scatter in the data is most likely due to differences in sedimentation and orientation of the fibrils. The effect of orientation and sedimentation on the measurement was attempted to be circumvented by mixing in-between each measurement. From figure 2 it is however evident that the suspension is shear thinning. The reason for the large increase of the viscosity at $\dot{\gamma} = 200 s^{-1}$ is that the flow in the cylinder of the viscometer becomes turbulent.

The dashed vertical lines in figure 2 show the range of shear rates obtained at the wall in the present experiments. For the shear rates of the present study, the relative viscosity (μ_s/μ_f where the indices s and f indicate suspension and fluid, respectively) is measured to be between 1.8 and 2 and the shear thinning is thus in the order of 10% or less.

2.3. Image analysis

In total 213 experiments with 50 images in each experiment are presented in this work. The images were categorised by manual inspection of each individual image, and classified into six flow regimes: *laminar*, *weak primary instability*, *strong primary instability*, *weak secondary instability*, *strong secondary instability* and *turbulent*. In order to make the analysis unbiased, the order in which the images are shown to the individual categorising them was random, and the process was repeated several times to ensure consistency.

3. Theoretical consideration

3.1. Single phase flow

The flow in a curved rotating channel is described by the Navier-Stokes equation together with the continuity equation in cylindrical coordinates as;

$$\frac{Du_r}{Dt} - \frac{u_\theta^2}{r} = -\frac{1}{\rho} \frac{\partial p}{\partial r} + \nu \left[\nabla^2 u_r - \frac{u_r}{r^2} - \frac{2}{r^2} \frac{\partial u_\theta}{\partial \theta} \right] + 2u_\theta \Omega, \quad (3)$$

$$\frac{Du_\theta}{Dt} + \frac{u_r u_\theta}{r} = -\frac{1}{\rho r} \frac{\partial p}{\partial \theta} + \nu \left[\nabla^2 u_\theta - \frac{u_\theta}{r^2} + \frac{2}{r^2} \frac{\partial u_r}{\partial \theta} \right] - 2u_r \Omega, \quad (4)$$

$$\frac{Du_z}{Dt} = -\frac{1}{\rho} \frac{\partial p}{\partial z} + \nu \nabla^2 u_z, \quad (5)$$

$$\frac{\partial u_r}{\partial r} + \frac{u_r}{r} + \frac{1}{r} \frac{\partial u_\theta}{\partial \theta} + \frac{\partial u_z}{\partial z} = 0, \quad (6)$$

where;

$$\frac{D}{Dt} = \frac{\partial}{\partial t} + u_r \frac{\partial}{\partial r} + \frac{u_\theta}{r} \frac{\partial}{\partial \theta} + u_z \frac{\partial}{\partial z}, \quad (7)$$

$$\nabla^2 = \frac{\partial^2}{\partial r^2} + \frac{1}{r} \frac{\partial}{\partial r} + \frac{1}{r^2} \frac{\partial^2}{\partial \theta^2} + \frac{\partial^2}{\partial z^2}, \quad (8)$$

and the velocity vector is given by;

$$\mathbf{u} = u_r \mathbf{e}_r + u_\theta \mathbf{e}_\theta + u_z \mathbf{e}_z. \quad (9)$$

The boundary conditions are;

$$u_r(r) = u_\theta(r) = u_z(r) = 0 \quad \text{at} \quad r = Ra \pm \frac{1}{2}d. \quad (10)$$

Assuming that $u_\theta = V(r)$ and $u_r = u_z = 0$ for the mean flow, together with equation 3 results in;

$$-\frac{V^2}{r} = -\frac{1}{\rho} \frac{\partial p}{\partial r} + 2V\Omega. \quad (11)$$

The mean velocity, given in Matsson & Alfredsson (1990), is obtained as a perturbation series in $\gamma = d/Ra$ as;

$$V = \frac{3}{2}(1 - \eta^2)\left(1 - \frac{1}{2}\gamma\eta\right) + \mathcal{O}(\gamma^2), \quad (12)$$

where η is the dimensionless spanwise coordinate defined by $r = Ra(1 + \frac{\gamma}{2}\eta)$, Assuming perturbations of the form;

$$u'_r = R(r)e^{i\beta z + st} \quad (13)$$

$$u'_\theta = \Theta(r)e^{i\beta z + st} \quad (14)$$

$$u'_z = Z(r)e^{i\beta z + st} \quad (15)$$

$$\frac{p'}{\rho} = P(r)e^{i\beta z + st}, \quad (16)$$

where β is the spanwise wavenumber and s the temporal growth rate, the linear stability equations are derived. Using the narrow gap approximation, $\gamma \ll 1$ and thus neglecting terms of order γ^2 and higher, this results in the following system of equations;

$$\begin{aligned} 4(D^2 - \beta^2)^2(1 + \gamma\eta)R + 4\gamma D(D^2 - \beta^2)R - 2\beta^2 \text{Re}(\gamma\mathcal{V} + \text{Ro}(1 + \frac{\gamma}{2}\eta))\Theta = \\ = 2s\text{Re}(D^2 - \beta^2)(1 + \gamma\eta) + s\text{Re}\gamma DR + \mathcal{O}(\gamma^2), \end{aligned} \quad (17)$$

$$\begin{aligned} 4(D^2 - \beta^2)(1 + \gamma\eta)\Theta + 2\gamma D\Theta - \text{Re}(2\mathcal{V}' + 4\text{Ro})(1 + \gamma\eta)R - \text{Re}\gamma\mathcal{V}R = \\ = 2s\text{Re}\Theta + \mathcal{O}(\gamma^2), \end{aligned} \quad (18)$$

where $D = \partial/\partial\eta$, and \mathcal{V} is the non-dimensional velocity.

Equations (17) and (18) constitute an eigenvalue problem for the unknown temporal growth rate s for a given triplet of Re , Ro and β . For each combination of (Re, Ro) , β can be varied so that the most unstable spanwise wavenumber is found and repeating at another (Re, Ro) combination, the stability in the Re/Ro -plane can be mapped out.

3.2. Effect of fibrils

When fibrils are added to the flow, this causes extra terms to appear in the stress tensor. Several studies has been carried out to derive an expression for these terms, either derived using slender body theory Batchelor (1970), Shaqfeh & Fredrickson (1990) or via continuum mechanics Ericksen (1960), Lipscomb II *et al.* (1988). The final expression in all cases, assuming weak Brownian motion, dilute concentration and large aspect ratios, takes the form;

$$\sigma = -p\delta_{ij} + 2\mu\varepsilon + \mu_{fibril}\varepsilon \langle \mathbf{p}\mathbf{p}\mathbf{p}\mathbf{p} \rangle, \quad (19)$$

where μ is the viscosity of the suspending fluid, $\mu_{fibril} = A\Phi$ is a rheological parameter dependent on concentration and aspect ratio, ε is the strain rate tensor and \mathbf{p} is the orientation vector for the fibril. In a semi-dilute suspension of rigid fibres Batchelor (1971) derived the following expression for A ;

$$A = \frac{r_p^2}{3\ln(\sqrt{2\pi}/\Phi)} \quad (20)$$

where r_p is the aspect ratio of the fibrils.

In order to calculate the fourth order orientation tensor, $\mathbf{a}_4 = \langle \mathbf{p}\mathbf{p}\mathbf{p}\mathbf{p} \rangle$, Advani & Tucker III (1987), an equation involving the sixth order orientation tensor \mathbf{a}_6 needs to be solved, and so on for higher moments. This problem is analogous to the well known closure problem of the Reynolds stresses in turbulence modelling. A closure approximation is needed in order to close the problem. Petrie (1999) discusses several of the available possibilities. In this paper however, the choice of closure approximation is avoided by assuming a stationary orientation distribution. In the first approximation it is assumed that all fibrils are performing orbits in the $r\theta$ -plane as described by Jeffery (1922) for simple shear. Through this assumption, the fibril orientation distribution is acquired by describing the angular velocity of the fibres by;

$$\dot{\varphi} = -\frac{\dot{\gamma}}{r_p^2 + 1}(r_p^2 \sin^2 \varphi + \cos^2 \varphi), \quad (21)$$

where φ is the angle between the fibril and the flow direction. The orientation distribution, Ψ , is found by solving the Smoluchowski equation, *e.g.* Doi & Edwards (1986);

$$\frac{\partial}{\partial \varphi}(\dot{\varphi}\Psi - C_l \dot{\gamma} \frac{\partial \Psi}{\partial \varphi}) = 0, \quad (22)$$

where C_l is an interaction coefficient modelling the interactions between the fibres causing rotary diffusion. Based on the orientation distribution it is possible to directly calculate all the elements in the orientation tensor \mathbf{a}_4 . For the second approximation another type of Jeffery orbits are assumed where all fibres have an orientation parallel to the z -axis, resulting in that all elements except $a_{zzzz} = 1$ in the orientation tensor is zero. In general the elements in the orientation tensor are calculated using the orientation vector;

$$p_r = \sin \xi \sin \varphi, \quad (23)$$

$$p_\theta = \sin \xi \cos \varphi, \quad (24)$$

$$p_z = \cos \xi, \quad (25)$$

where ξ is the angle between the shear plane and the fibre axis. For a given orientation distribution, the elements of a_{ijkl} are readily calculated.

Figure 3 shows the shear viscosity predicted by this model varying the parameters r_p , C_l and Φ . It is clear that the relative viscosity found in the viscometer (1.8–2, see figure 2) can be reached by different parameter combinations. Note that interaction parameter C_l must be shear dependent in order for the model to become shear thinning.

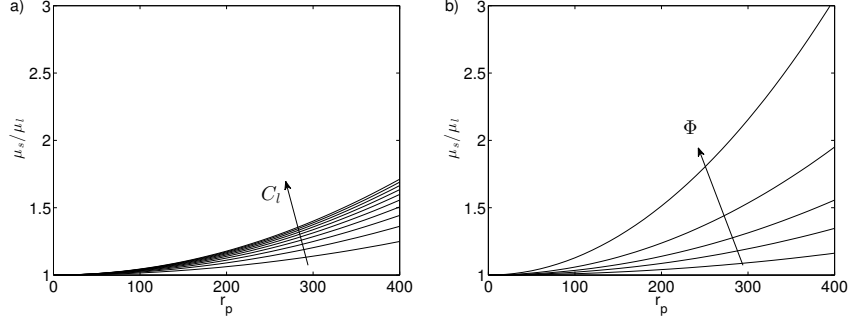


FIGURE 3. Effects of parameters on the rheological model used. In both a) and b) the effective viscosity, μ_s/μ_l , is shown versus the aspect ratio r_p . In a) the volume fraction, $\Phi = 3.08 \cdot 10^{-4}$, is kept constant and the interaction coefficient is varied in the interval $C_l = [0.01, 0.1]$. In b) the interaction coefficient is kept constant at $C_l = 0.05$ and the volume fraction is varied with the values $\Phi = 10^{-4} \cdot 2 \cdot 10^{-4} \cdot 3.08 \cdot 10^{-4} \cdot 5 \cdot 10^{-4} \cdot 10^{-3}$

The final stability equation taking fibrils into consideration takes the following form;

$$\begin{aligned}
& 4(D^2 - \beta^2)^2(1 + \gamma\eta)R + 4\gamma D(D^2 - \beta^2)R - 2\beta^2 \text{Re}(\gamma\mathcal{V} + \text{Ro}(1 + \frac{\gamma}{2}\eta))\Theta + \\
& + A\Phi \left[4a_{rrrr}\beta^2 D^2(1 + \gamma\eta)R + 2\gamma a_{rrrr}\beta^2 DR + \right. \\
& \left. + 4a_{rrr\theta}\beta^2 D^2(1 + \gamma\eta)\Theta - 2\gamma a_{r\theta\theta\theta}\beta^2 D\Theta - 2a_{zzzz}\beta^2(\gamma D + 2D^2(1 + \gamma\eta)) \right] = \\
& = 2s \text{Re}(D^2 - \beta^2)(1 + \gamma\eta)R + \gamma s \text{Re}DR + \mathcal{O}(\gamma^2), \tag{26}
\end{aligned}$$

$$\begin{aligned}
& 4(D^2 - \beta^2)(1 + \gamma\eta)\Theta + 2\gamma D\Theta - \text{Re}(2\mathcal{V}' + 4\text{Ro})(1 + \gamma\eta)R - \gamma \text{Re}\mathcal{V}R + \\
& + A\Phi \left[4a_{rrr\theta}D^2(1 + \gamma\eta)R + 4\gamma a_{rrr\theta}DR + 2\gamma a_{r\theta\theta\theta}DR + 4a_{rr\theta\theta}D^2(1 + \gamma\eta)\Theta \right] = \\
& = 2s \text{Re}(1 + \gamma\eta)\Theta + \mathcal{O}(\gamma^2), \tag{27}
\end{aligned}$$

where a_{ijkl} are the (possible) non-zero elements in the fourth order orientation tensor. The two equations above constitute an eigenvalue problem that is treated as described for the single phase above.

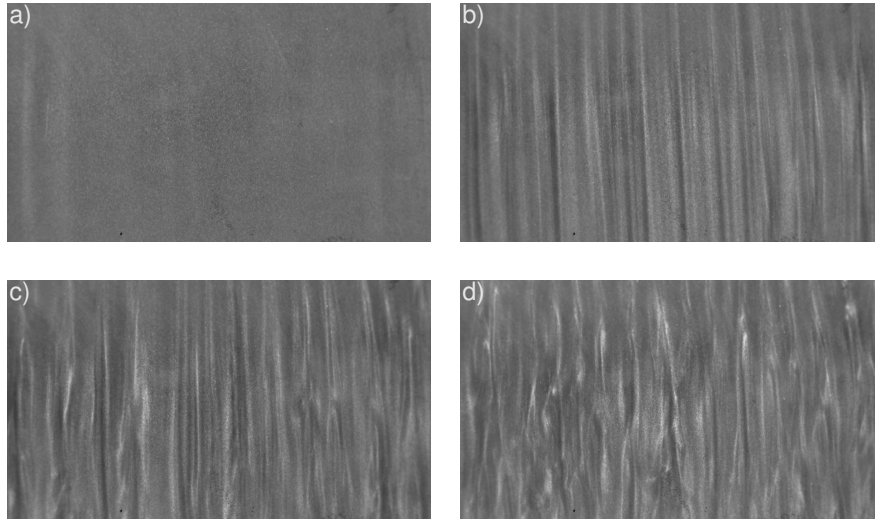


FIGURE 4. Example images for a) laminar, b) strong primary, c) weak secondary and d) strong secondary regimes, with $Re=595$, $Ro = -0.39 \cdot 10^{-3}$, $0.1 \cdot 10^{-3}$, $0.64 \cdot 10^{-3}$ and $1.27 \cdot 10^{-3}$.

4. Results

4.1. Experimental results

The images of the flow are analysed by visual inspection and thereby each case is assigned a different regime. In figure 4, example images from four different regimes at a constant Reynolds number ($Re=595$) are shown for different rotational numbers ($Ro = -0.39 \cdot 10^{-3}$, $0.1 \cdot 10^{-3}$, $0.64 \cdot 10^{-3}$ and $1.27 \cdot 10^{-3}$), the flow is from top to bottom in the images. As is evident from the images, the difference between figure 4a and figure 4b is very distinct, the transition from laminar flow to the primary instability is therefore well defined. The two following transitions (from primary to weak secondary and continuing to strong secondary) are less obvious.

In figure 5, the results from the visual inspection has been summarised in two plots showing the regime each case belongs to for pure water in (a) and the NFC suspension in (b). The Reynolds number in the two figures is based on the viscosity of water. The laminar region (\circ) extends up to the highest Re at $Ro \approx -0.03$. At this rotation rate, the centrifugal (from curvature) and Coriolis (from rotation) forces balance each other and stabilises the flow the most. If Ro is decreased further from this value, Coriolis driven instabilities dominate. For higher Ro , the curvature effects dominate. Note that for $Ro > 0$,

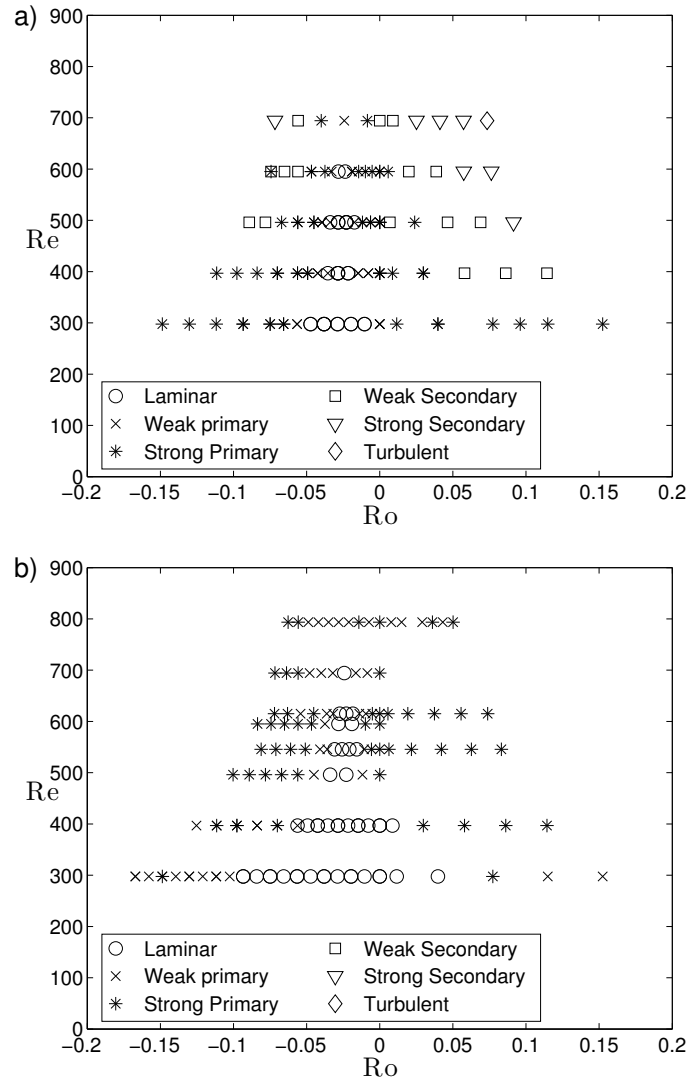


FIGURE 5. State diagrams for a) pure water and b) NFC suspension. The Reynolds number is in both figures based on the viscosity of water.

the centrifugal and Coriolis forces interact and destabilise the flow also for low rotation rates.

Comparing figure 5 a) and b), the NFC clearly stabilises the flow: the laminar region is greater and there are no secondary instabilities observed in the

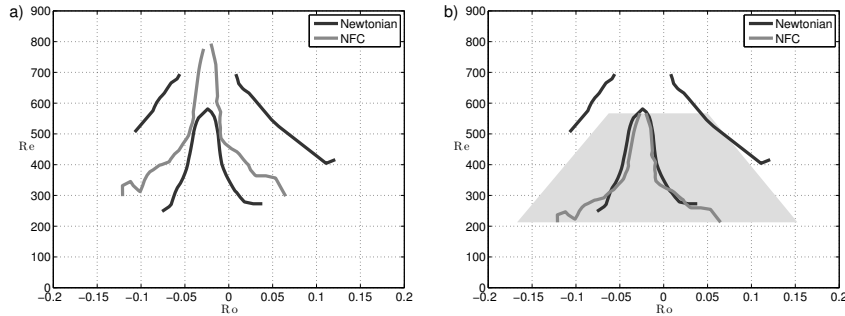


FIGURE 6. Contours showing a) the onset of the primary and secondary instability in the experiments where the Reynolds number is based on the viscosity of water and b) the onset of the primary and secondary instability in the experiments where the Reynolds number has been scaled by a factor of 1.4 for the NFC suspension, the shaded area indicates the location of the experiments for the NFC suspension.

studied parameter space. Figure 6a depicts the contours of the first (from laminar to primary instability) and second transition (from primary to secondary instability) for the case of the pure water as well as the NFC suspension. In figure 6b, the Reynolds number for the NFC suspension has been scaled with a factor of 1.4, that seems to make the peaks assume a similar value. From a stability perspective, this can be viewed as an approximation of the effective viscosity in the experiments.

Also note that the shadowed region in figure 6b indicate the parameter space spanned with the NFC-suspension. This area only touches the secondary transition and thus, the only conclusions regarding the onset of the secondary instability with NFC that can be made is that the secondary instability does not seem to be enhanced.

4.2. Linear stability results

In figure 7 results from the linear stability analysis are shown as the neutral stability curve in the Re-Ro-plane for different volume fractions of fibrils, $\Phi = 0.000308$ correspond to the amount used in the experiments. The aspect ratio ($r_p = 340$) and interaction coefficient ($C_l = 0.05$) has been chosen such that the effective viscosity is equal to $\mu_s/\mu_l = 1.4$ at the concentration of the experiments. This corresponds well to what can be seen in figure 6b. In figure 7a, the fibres are assumed to perform Jeffery orbits in the shear plane. Figure 7b shows the neutral stability curve from linear stability theory considering all fibres to have an orientation parallel to the z -axis.

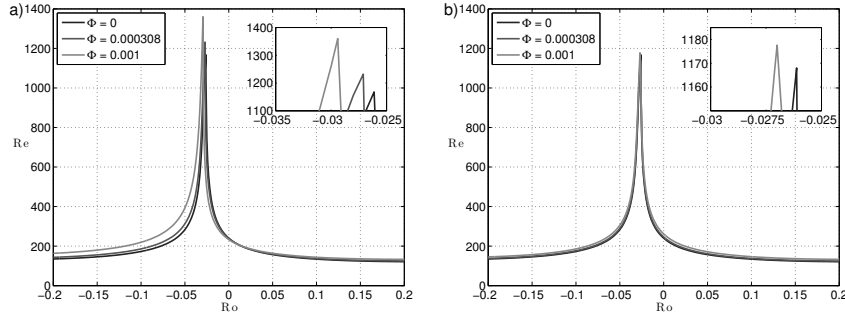


FIGURE 7. Contours showing primary instability obtained by linear stability analysis with different volume fractions, Φ , of fibrils considering in a) that the fibres are performing Jeffery orbits in the shear plane and in b) that all fibres are have an orientation parallel to the z -axis. Here an aspect ratio of $r_p = 340$ and an interaction coefficient $C_l = 0.05$ are used.

The effects of the fibrils are stronger in figure 7a than in 7b. However, also in 7a the effect on the maximum critical Reynolds number is less than 10% when comparing pure water ($\Phi = 0$, the black curve) with the experimental $\Phi = 0.000308$ (see the inset). At $\Phi = 0.001$ (where the relative viscosity is around 2.5, see figure 3b), the effect on the critical Re is still less than 15%. In the experiments, the difference was 40%, since the scaling factor in figure 6b is 1.4.

5. Discussion

The results show that neither viscometer rheology characterisation nor the linear stability calculations predict the effect of the fibrils on stability correctly. The experimental results showed that critical curves in the Re/Ro-plane for pure water and the NFC suspension collapsed when the Re (i.e. viscosity) of the NFC suspension was scaled with a factor 1.4. This factor is considerable smaller than that predicted by the viscometer measurements "1.8–2" and considerable larger than what is obtained from the linear stability theory "1.1". However, that the qualitative behaviour is the same; the effect of the fibrils on the bulk viscosity is greater than on the stability, both for the experiments (viscometer and flow visualisations) and for the theoretical consideration (figures 3 and 7).

These quantitative differences will be discussed in the light of the orientation distribution of the fibrils. In the experiments, there is a strong contraction prior to the flow channel. Thus, it can be assumed that the fibrils are aligned in the flow direction when exposed to the accelerated flow at the inlet of the channel. Exposed to the shear in the channel, the fibres will perform Jeffery orbits as described by equation (21). The orientation distribution should then

be fairly well described by the one resulting in figure 7a. As mentioned, the effects of fibrils is under-predicted in figure 7a.

However, as the flow rolls are formed, the actual orientation distribution will change. This aspect has not been included in the present analysis. To what extent this feature will explain the difference between observed and predicted behaviour is left for future works. Unfortunately, such an effort will rely on a closure model and therefore, one additional parameter enters the analysis. An alternative approach would be to perform simulations that rely on first principles to a larger extent.

When it comes to the viscometer, the orientation distribution is more random in the viscometer as compared to what can be expected in the flow channel, assuming alignment in the contraction. It is clear that if quantitative comparisons between rheology measurements, experiments and theoretical considerations are to be made, the orientation distributions have to be determined to an extent that may be unfeasible. The present flow system provides a stability mapping in the ReRo-plane. Thus, effects of different parameters (Φ, C_l, r_p) is obtained as a curve rather than a point. Consequently, effects, causes and predictability are explored with increased precision, in spite of the elusive orientation distribution.

6. Conclusions

Stability of an NFC-suspension flowing in a curved and rotating channel has been studied. The main conclusions are;

- The primary instability is stabilised as NFC is added.
- The increase of the critical Reynolds number is less than what could be expected from the effective viscosity measured by a viscometer.
- Linear stability theory assuming a constant orientation distribution under predicts the stabilising effect of the NFC.
- The secondary instability does not seem to be enhanced by the presence of the fibrils.

The conclusions highlight the difficulties inherent in modelling and predicting unsteady behaviour of NFC-suspension flow. This is consistent with previous observations of polymer and fibre suspension flows. However, the present experiment provides a complete stability map and thus, qualitative comparisons can be made. Here, the relative difference between effective bulk viscosity over the change in critical Reynolds number are surprisingly similar: $1.8/1.4 \approx 1.3$ in the experiments and $1.4/1.1 \approx 1.3$ in the theoretical consideration.

References

- ADVANI, S. G. & TUCKER III, C. L. 1987 The use of tensors to describe and predict fiber orientation in short fiber composites. *Journal of Rheology* **31** (8), 751–784.
- AZAIÉZ, J. 2000 Linear stability of free shear flows of fibre suspensions. *Journal of Fluid Mechanics* **404**, 179–209.
- BATCHELOR, G. K. 1970 The stress system in a suspension of force-free particles. *Journal of Fluid Mechanics* **41** (03), 545–570.
- BATCHELOR, G. K. 1971 The stress generated in a non-dilute suspension of elongated particles by pure straining motion. *Journal of Fluid Mechanics* **46** (04), 813–829.
- DOI, M. & EDWARDS, S. F. 1986 *The Theory of Polymer Dynamics*. Oxford University Press.
- ERICKSEN, J. 1960 Transversely isotropic fluids. *Colloid & Polymer Science* **173**, 117–122.
- FALL, A. B., LINDSTRÖM, S. B., SUNDMAN, O., ÖDBERG, L. & WÅGBERG, L. 2011 Colloidal stability of aqueous nanofibrillated cellulose dispersions. *Langmuir* **27** (18), 11332–11338.
- GUPTA, V. K., SURESHKUMAR, R., KHOMAMI, B. & AZAIÉZ, J. 2002 Centrifugal instability of semidilute non-brownian fiber suspensions. *Physics of Fluids* **14** (6), 1958–1971.
- IOTTI, M., GREGERSEN, O. Y., MOE, S. R. & LENES, M. 2011 Rheological studies of microfibrillar cellulose water dispersions. *Journal of Polymers and the Environment* **19**, 137–145.
- JEFFERY, G. B. 1922 The motion of ellipsoidal particles immersed in a viscous fluid. *Proceedings of the Royal Society of London. Series A, Containing Papers of a Mathematical and Physical Character* **102** (715), pp. 161–179.
- LIPSCOMB II, G., DENN, M., HUR, D. & BOGER, D. 1988 The flow of fiber suspensions in complex geometries. *Journal of Non-Newtonian Fluid Mechanics* **26** (3), 297 – 325.
- MATSSON, O. J. E. & ALFREDSSON, P. H. 1990 Curvature- and rotation-induced instabilities in channel flow. *Journal of Fluid Mechanics* **210**, 537–563.
- NSOM, B. 1996 Stability of fiber suspension flow in curved channel. *Journal de Physique II* **6** (10), 1483–1492.
- PÄÄKKÖ, M., ANKERFORS, M., KOSONEN, H., NYKÄNEN, A., AHOLA, S.,

- ÖSTERBERG, M., RUOKOLAINEN, J., LAINE, J., LARSSON, P. T., IKKALA, O. & LINDSTRÖM, T. 2007 Enzymatic hydrolysis combined with mechanical shearing and high-pressure homogenization for nanoscale cellulose fibrils and strong gels. *Biomacromolecules* **8** (6), 1934–1941.
- PETRIE, C. J. 1999 The rheology of fibre suspensions. *Journal of Non-Newtonian Fluid Mechanics* **87** (2-3), 369 – 402.
- PILIPENKO, V. N., KALINICHENKO, N. M. & LEMAK, A. S. 1981 Stability of the flow of a fiber suspension in the gap between coaxial cylinders. *Soviet Physics Doklady* **26**, 646.
- PUISTO, A., ILLA, X., MOHTASCHEMI, M. & ALAVA, M. J. 2012 Modeling the viscosity and aggregation of suspensions of highly anisotropic nanoparticles. *European Physics Journal E* **35** (1), 6.
- SHAQFEH, E. S. G. & FREDRICKSON, G. H. 1990 The hydrodynamic stress in a suspension of rods. *Physics of Fluids A: Fluid Dynamics* **2** (1), 7–24.
- VASELESKI, R. C. & METZNER, A. B. 1974 Drag reduction in the turbulent flow of fiber suspensions. *AIChE Journal* **20** (2), 301–306.
- ZHENJIANG, Y., JIANZHONG, L. & ZHAOSHENG, Y. 2004 Hydrodynamic instability of fiber suspensions in channel flows. *Fluid Dynamics Research* **34** (4), 251 – 271.